RESEARCH ARTICLE | OCTOBER 04 2024

Determining the chemical ordering in nanoalloys by considering atomic coordination types

Riccardo Farris ; Konstantin M. Neyman ; Albert Bruix

J. Chem. Phys. 161, 134114 (2024)
https://doi.org/10.1063/5.0214377

The Journal of Chemical Physics ARTICLE pubs.aip.org/aip/jcp

Determining the chemical ordering in nanoalloys by considering atomic coordination types

Cite as: J. Chem. Phys. 161, 134114 (2024); doi: 10.1063/5.0214377
Submitted: 17 April 2024 • Accepted: 25 August 2024 •
Published Online: 4 October 2024

Riccardo Farris,[1] Konstantin M. Neyman,[1,2] and Albert Bruix[1,a)]

AFFILIATIONS

[1] Departament de Ciència de Materials i Química Física and Institut de Química Teòrica i Computacional (IQTC-UB), Universitat de Barcelona, 08028 Barcelona, Spain
[2] ICREA (Institució Catalana de Recerca i Estudis Avançats), 08010 Barcelona, Spain

[a)] **Author to whom correspondence should be addressed:** abruix@ub.edu

ABSTRACT

The energetically most favorable chemical ordering of bimetallic nanoparticles can be characterized by combining global optimization algorithms and surrogate energy models. The latter approximate the energy of nanoalloys relying on structural descriptors, training models, and data. Here, we systematically evaluate the performance of highly data-efficient topological descriptors [Kozlov *et al.*, Chem. Sci. **6**, 3868 (2015)] for predicting the energies of metal nanoalloys with different chemical orderings. We also introduce a new descriptor based on atomic coordination types, which results in a less data-efficient and interpretable approach, but improves the general accuracy and the quantification of orderings in the inner parts of nanoparticles. The capacity of both the original and new approaches in combination with a basin hopping algorithm is illustrated by generating convex hulls of PdZn nanoalloys and predicting the resulting active surface site distribution as a function of particle composition. Finally, we show how these approaches can be combined with machine-learning adsorption models in electrocatalysis studies for a fast evaluation of the reactivity landscape of targeted nanoalloys.

I. INTRODUCTION

Metal nanoparticles (NPs) attract significant attention due to their tunable properties[1,2] and multiple applications in fields such as optics,[3] magnetism,[4] and catalysis.[5] The properties of these NPs depend on their size, shape, and composition.[1–5] They can thus also be modified by combining different metals. NPs formed of two or more metals are referred to as nanoalloys. Their properties are defined not only by their size, morphology,[6] and composition, but also by their chemical ordering,[7] i.e., the particular arrangement of atoms of the different metal elements within the NP lattice.

The structural complexity of nanoalloys makes it challenging to construct representative structural models and reliably calculate the resulting physical and chemical properties. Experimental information regarding particle size and shape of the nanoalloy of interest is often available, but the chemical ordering within such particles is more elusive. Therefore, for nanoalloys exhibiting a known particle shape, size, and crystalline structure, the challenge of deriving a representative structural model is simplified to finding the most stable arrangement of atoms of different metals in inequivalent positions of the crystalline particle.

For an A_mB_n particle composed of m A and n B atoms, there are (m + n)!/m!n! isomers differing only in the chemical ordering (called *homotops*[1]). This amounts to ~10^{58} possible chemical orderings (including symmetry-equivalent ones) for an $A_{100}B_{100}$ particle, making a comprehensive exploration of the configurational space of chemical orderings unfeasible. Fortunately, one is often interested only in several energetically most stable chemical orderings. Such structures can be identified by means of Global Optimization (GO) methods[1] that efficiently explore the search space, systematically identifying the (ideally most) stable structures. Despite the improved computational efficiency of GO algorithms with respect to comprehensive or randomized searches, these algorithms still require carrying out energy evaluations of hundreds to millions of candidate structures, even for systems comprising a quite small number of atoms. This precludes the use of costly *ab initio* calculations such as those based on the Density Functional Theory (DFT) directly in combination with GO algorithms. Therefore, one must rely on

lower-accuracy approximations or surrogate energy models (SEMs). The two main ingredients of a GO approach are thus the search algorithm and the approximation used to calculate the energy of each evaluated candidate structure.

Different GO algorithms exist to determine the structure of metal particles, including Monte Carlo (MC) simulations,[8–11] Basin Hopping (BH),[12] or Genetic Algorithm (GA).[13–15] In turn, several energy models have been developed to approximate the energy of nanoalloy structures with low computational costs. Many studies[10,16–19] have relied on empirical or semiempirical approximations, such as the Gupta[20] and EMT[21]/EAM[22] interatomic potentials. More recently, machine-learning (ML) interatomic potentials have also been developed and applied to nanoalloy characterization.[23–26] Such ML potentials are usually parameterized to reproduce first-principles data and rely on both a learning method (e.g., regressions or neural networks) and the so-called descriptors.[27–33] The latter are alternative representations of the atomic coordinates suitable for parameterizing and applying the resulting energy expression, which is often referred to as the aforementioned SEM.

Other SEMs involve simpler descriptors that account for occurrences of certain bonds, atoms with given coordination numbers, or clusters of atoms. Mpourmpakis and co-authors developed bond-centric models[34–36] using bond dissociation energies and bulk cohesive energies to approximate the NP formation energies, which were combined with a GA to find the global minimum of targeted alloys. The coordination-based model proposed by Roling *et al.*[37–39] relied on a parameterization of the contributions to the nanoalloy formation energies from atoms of the two elements with different coordination numbers. The more complex (and accurate) Cluster Expansion (CE)[40–46] approaches have been applied to, for example, O/PtRu,[47] AuAg,[46] or O/PtCu[43] alloy modeling studies.

In this study, we focus on the *topological* (TOP) method[48,49] introduced by one of us and considered a reliable and data-efficient method to optimize the chemical ordering of bimetallic NPs.[50–59] The original TOP formulation used a SEM based on so-called topological descriptors accounting for occurrences of heterometallic bonds and atoms with different coordination numbers. Here, we conduct a comprehensive evaluation of the performance of the TOP descriptors using workflows from ML approaches, focusing on the learning curves, parameter interpretability, and accuracy for PtAu, PtCu, and PdZn nanoalloys.[60]

By addressing the interpretability of the resulting parameters, data-efficiency, and accuracy of the descriptors, we aim to advance the understanding and predictive capabilities for these technologically significant nanoalloys with diverse chemical bonding. In addition, we introduce a new descriptor for nanoalloys based on atomic coordination types (ACTs) and evaluate its performance, providing a robust framework for future nanoalloy research.

The selection of these specific nanoalloys is motivated by their distinct stable chemical orderings and their technological relevance, particularly in catalysis. PtAu nanoalloys [Fig. 1(a)], which are stable in a core(Pt)–shell(Au) chemical ordering, have demonstrated significant catalytic activity in methanol oxidation, hydrogenation reactions, and the reduction of organic compounds, showing improved results upon alloying.[61–63] PtCu nanoalloys [Fig. 1(b)], exhibiting a stable mixed chemical ordering, have shown enhanced catalytic properties in ethanol oxidation, CO oxidation, and oxygen reduction reactions.[64–66] PdZn nanoalloys [Fig. 1(c)], belonging to intermetallic systems with very strong Pd–Zn bonds and stable in a layered chemical ordering (L10), have shown an improved performance in methanol oxidation reactions compared to pure Pd catalysts.[67] They possess properties similar to Cu nanoparticles, making them attractive alternatives for methanol synthesis and steam reforming,[68] and are used for selective hydrogenation of organic compounds.[69]

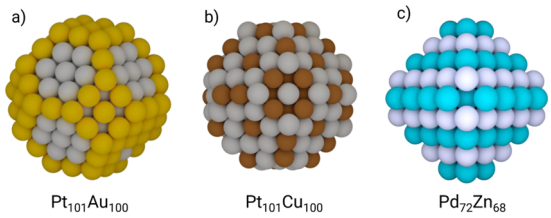

FIG. 1. The most stable calculated chemical ordering of the (a) $Pt_{101}Au_{100}$ nanoparticle, depicted in gray (Pt) and yellow (Au), (b) $Pt_{101}Cu_{100}$ nanoparticle, depicted in gray (Pt) and brown (Cu) and (c) $Pd_{72}Zn_{68}$ nanoparticle, depicted in cyan (Pd) and silver (Zn).

II. METHODS

A. Computational details of DFT and effective medium theory calculations

In this work, we calculated the total energy of bimetallic NPs using either Effective Medium Theory (EMT) potentials[21] or DFT methods. EMT calculations were carried out using the "*as soon as possible*" calculator implemented in the Atomic Simulation Environment (ASE) Python library.[70] EMT calculations are less reliable than DFT calculations, but their much lower computational cost allows us to generate databases with many structures and energies of bimetallic NPs under study. We use these large databases to evaluate the accuracy of surrogate energy models based on different descriptors. We have also created databases with fewer structures of a touchstone PdZn system for which nanoparticle energies were calculated by DFT. All such DFT calculations were performed with the periodic plane wave code VASP.[71,72] A Perdew–Burke–Ernzerhof (PBE) exchange–correlation functional[73] was employed, which is considered one of the most accurate semi-local functionals for properties of transition metal bulk and surfaces.[74–76] The projector augmented wave (PAW) method was used to describe the interaction between valence electrons and the fixed core electron densities.[77,78] The valence electrons were expanded with plane wave basis sets with a kinetic energy cutoff of 415 eV. The Brillouin zone was sampled only at the Γ-point. One-electron Kohn–Sham levels were smeared by 0.1 eV, and the converged total energies were finally extrapolated to zero smearing. The electronic structure was self-consistently calculated until energy differences between consecutive steps were smaller than 10^{-6} eV. The NP structures calculated using EMT and DFT methods were relaxed until all forces acting on each atom became less than 0.02 eV/Å. The 140-atom PdZn NPs were placed in periodically repeated cubic cells of $2.3 \times 2.3 \times 2.3$ nm^3, allowing a separation >0.7 nm between them. At such distances, interaction of metal particles with their periodic images is negligible for the purpose of this work.[79,80]

B. Surrogate energy models for solving the chemical ordering problem

Surrogate Energy Models (SEMs) are becoming increasingly popular as a computationally efficient alternative to expensive *ab initio* calculations for determining the energy of molecular or condensed matter systems.[81,82] These models rely on representations of the system structure derived from atomic coordinates, known as descriptors, and a function that maps the energy of the system to these descriptors. To develop a parameterized function for the SEM, a dataset of structures and their corresponding energies calculated at the desired level of theory is required. As such, the SEM is defined by the dataset of structures and energies, the descriptors used to represent the structures, and the function or model used for mapping the relationship between the descriptor and the energy.

C. Descriptors for alloy nanoparticles

To be used effectively in SEMs, descriptors should ideally be unique and invariant to system rotation, translation, and permutation of equivalent atoms. Descriptors should also be computationally efficiently calculated and easy to store. They replace the 3N-dimensional coordinates of a given N-atomic system with a feature vector of dimension equal to the number of features or model parameters used. Descriptors are commonly categorized as either local or global. Local descriptors are divided into contributions from each atom in the system, resulting in a high-dimensional descriptor vector that encodes the surrounding of each atom independently. This approach allows learning both global properties, such as the energy of the system as the sum of atomic contributions, and local properties, such as atomic forces and charges. Meanwhile, global descriptors encode information for all atoms in the system as a whole, leading to lower-dimensional descriptor vectors, but limited to global properties. Global descriptors are particularly useful for SEMs for the chemical ordering problem in alloys, where the objective is to accurately approximate the energy of the whole system rather than of particular atoms of the system. Examples of global descriptors include the above-mentioned bond-centric[34–36] or coordination-based models,[37–39] cluster expansion approaches,[40–46] and also the TOP and ACT descriptors discussed in this work. We note that, in this work, we focus on nanoalloys exhibiting fcc-type packing, but the underlying principles of the TOP and ACT energy models can be extended to other packing motifs such as hcp, bcc, and even amorphous structures (as long as first neighbors can be reliably defined).

D. Topological descriptors

The topological (TOP) descriptors[49] are used to depict the chemical ordering of two distinct metal elements in a bimetallic NP with given atomic lattice positions. The descriptors encompass global characteristics, including the amounts of homo- and heterometallic bonds and of atoms of each element in positions with differing coordination.[28] The original formulation of the TOP descriptors represented bimetallic NPs comprising A and B atoms as

$$N^{TOP} = \left[N^{AB}, N^{A,CORNER}, N^{A,EDGE}, N^{A,TERRACE}\right], \quad (1)$$

where N^{AB} is the number of heterometallic bonds and $N^{A,CORNER}, N^{A,EDGE}$, and $N^{A,TERRACE}$ are the numbers of atoms of one of the two elements (A) that occupy the corresponding positions in the *fcc*-type NP with coordination numbers of 6 for corner, 7 for edge, and 8 or 9 for terrace, respectively (Fig. 2). The SEM used in the TOP approach assumes a linear relationship between the energy of the system and each of the TOP descriptors. Therefore, the parameters of the linear function can be obtained through linear regression (see Sec. II F).

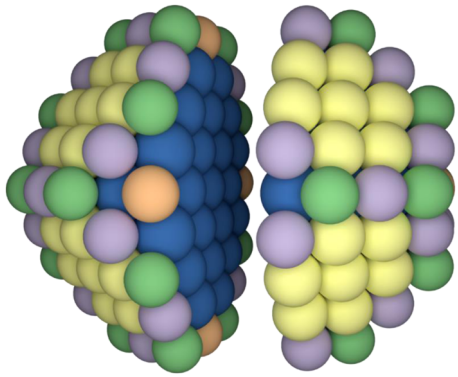

FIG. 2. Truncated octahedral fcc-type NP of 201 atoms color-coded according to their coordination numbers. The related N^{TOP} descriptor for different atomic orderings of A and B metals in this particle is obtained by counting the number of AA and AB bonds and the number of atoms of metal A with coordination numbers 12 (blue), 9 (yellow), 8 (orange), 7 (violet), and 6 (green), i.e., those occupying bulk, [111] facets, [100] facets, edge, and corner positions, respectively.

We note that N^{TOP} in Eq. (1) does not include all topological descriptors—a complete list would also include N^{BB}, N^{AA}, $N^{A,BULK}, N^{B,CORNER}, N^{B,EDGE}, N^{B,TERRACE}$, and $N^{B,BULK}$. The $N^{B,TERRACE}$ descriptors can be further separated into contributions from inequivalent particle facets (e.g., $N^{i,111}$ and $N^{i,100}$ representing terrace atoms with coordination numbers 8 and 9, respectively). However, most of the descriptors originally excluded from TOP are linearly correlated with the included ones and their inclusion would be superfluous. In turn, the inclusion of the non-linearly correlated descriptors such as N^{BB} or N^{AA} can improve the accuracy as shown below but often makes the resulting energy expression harder to interpret. Note that the descriptors used in bond-centric,[34–36] or coordination-based[37–39] models are subsets of the topological descriptors.

The main advantages of TOP descriptors are their simplicity, surface sensitivity (important, e.g., for catalytic applications), and low dimensionality, requiring only a small number of data points (i.e., training examples) to obtain well-converged parameters when training the SEM and generally representing well ordering of the NP surface. As a result, TOP descriptors can provide accurate enough energy approximations for optimizing the chemical ordering of various bimetallic nanoalloys with high data-efficiency (i.e., requiring a small number of first-principles calculations). For example, the predicted accuracy of the TOP descriptor for $Pt_{201-x}Au_x$ and $Pt_{201-x}Cu_x$ NPs is 0.96 and 2.47, meV/atom, respectively, requiring only 61 and 141 structures to converge the SEM parameters. However, there are inherent limitations for such a simple approach, in particular, a notable non-uniqueness of the TOP descriptors. That is, inequivalent chemical orderings can have the same $N^{AB}, N^{A,CORNER}, N^{A,EDGE}$,

and $N^{ATERRACE}$ values that define the so-called *topology*. This sometimes leads to a quite broad spread of relative energies among homotops with the same topology, which becomes increasingly important for larger NPs with many bulk-like (inner) atoms. Chemical ordering differences in such bulk regions are only accounted for by the number of homo- and heterometallic bonds, which are not capable of differentiating complex patterns, e.g., layered bulk structures. In addition, the TOP and related bond-centric models treat all bonds of the same type as equivalent, neglecting the ligand-like effects where the energy of an AB bond is affected by the bonds that the A and B atoms form to their other nearest-neighboring atoms.

Although the TOP descriptors have been used extensively for optimizing the chemical ordering of bimetallic nanoalloys, a thorough evaluation of their accuracy and transferability using established ML workflows (such as cross-validation and learning curves) is still lacking and we address it in this work.

E. A new descriptor based on atomic coordination types (ACTs)

We propose a new approach to represent nanoalloy structures, which aims to overcome some of the limitations of the TOP descriptors. Our approach is based on a classification of every atom of a nanoalloy into different atom-types, defined according to the coordination environment of the atom, and called hereafter as Atomic Coordination Types (ACTs). Each atom-type is characterized by the element identity and the number of homo- and heterometallic bonds it forms with the nearest-neighbor atoms, as illustrated in Fig. 3. The ACT descriptor then quantifies the number of occurrences of each atom-type in the system. Unlike the TOP descriptors, this approach accounts for the inequivalence between atoms with the same coordination numbers but different compositions of neighbor atoms, leading to a better differentiation of inequivalent chemical orderings in both surface- and bulk-like (inner) regions of nanoalloys. The ACT descriptor also takes into account ligand effects on bond contributions, partially accounting for the inequivalence between homometallic bonds or different heterometallic bonds. The complete ACT feature vector (i.e., the descriptor vector) is thus

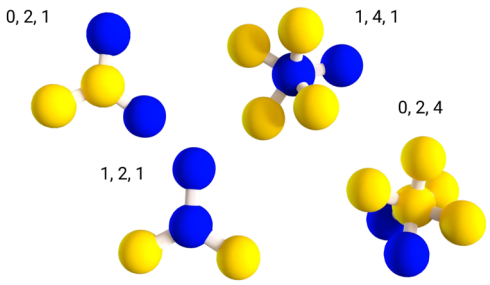

FIG. 3. Some atom-types and their s, n_{AA}, n_{AB} labels as defined in the ACT descriptor approach. The atom identity (s) has values between 0 and M–1, where M is the number of elements in the nanoparticle (2 for bimetallic alloys). The number of homometallic (n_{AA}) and heterometallic (n_{AB}) bonds the atom forms can take values from 0 to 12. The ACT descriptor is a vector with dimension equal to the number of atom types, in which the value of each element is the number of occurrences of the corresponding atom type.

$$\boldsymbol{N}^{ACT} = [N_{0,0,0}, N_{0,0,1}, N_{0,1,0}, N_{0,0,2}, N_{0,1,1}, N_{0,2,0}, \ldots, N_{s,n_{AA},n_{AB}}, \ldots, N_{1,12,0}], \quad (2)$$

where every atom-type $N_{s,n_{AA},n_{AB}}$ is defined by the element type, s, of the central atom (having values of 0 for metal A and 1 for metal B) and the number of homometallic (n_{AA}) and heterometallic (n_{AB}) bonds to atoms within the first coordination shell. Each atom-type contains the coordination number cn of the central atom, $cn = n_{AA} + n_{AB}$. The dimension of the complete $\boldsymbol{N}^{ACT}$ descriptor is 182 for atom types with coordination numbers ranging from 0 (unbound single atoms) to 12 (fully coordinated atoms). However, the descriptor vector dimension is significantly reduced by considering only the atom types relevant to the targeted NP structure. For example, for the truncated octahedral fcc-type NP shown in Fig. 2, $\boldsymbol{N}^{ACT}$ includes only terms corresponding to the cn 6, 7, 8, 9, and 12, resulting in a reduced dimension of 94. For the NPs depicted in Fig. 1, $\boldsymbol{N}^{ACT}$ would be

$$\begin{aligned}\boldsymbol{N}^{ACT} = [&N_{0,0,6}, N_{0,1,5}, \ldots, N_{0,0,6}, \ldots, N_{0,7,0}, \ldots, N_{0,0,7}, \ldots,\\ &\times N_{0,8,0}, \ldots, N_{0,0,8}, \ldots, N_{0,9,0}, \ldots, N_{0,0,9}, N_{0,12,0}, \ldots\ldots,\\ &\times N_{0,0,12}, N_{1,0,6}, N_{1,1,5}, N_{1,0,6}, \ldots, N_{1,7,0}, \ldots, N_{1,0,7}, \ldots,\\ &\times N_{1,8,0}, \ldots, N_{1,0,8}, \ldots, N_{1,9,0}, \ldots, N_{1,0,9}, N_{1,12,0}, \ldots, N_{1,0,12}].\end{aligned} \quad (3)$$

Although being significantly higher dimensional than the TOP descriptors, $\boldsymbol{N}^{ACT}$ is simpler than other popular global descriptors such as the Coulomb matrix[83] or many-body tensor representations.[84] The ACT descriptors are also more unique than the TOP ones. Namely, a multitude of homotops with different chemical orderings, but corresponding to the same TOP descriptors, is in general split in the ACT method into several groups, each corresponding to a distinct ACT descriptor. Similar to TOP models, the ACT models assume a linear dependence between the system's energy and each descriptor.

F. Linear regression models

The energy E_i^{TOP} of a NP structure i with the corresponding TOP feature vector $\boldsymbol{N}_i^{TOP}$ is obtained as

$$E_i^{TOP} = \varepsilon^{TOP} \boldsymbol{N}_i^{TOP}, \quad (4)$$

where ε^{TOP} is the fitted parameter vector of the model. The ACT energy E_i^{ACT} is analogously

$$E_i^{ACT} = \varepsilon^{ACT} \boldsymbol{N}_i^{ACT}. \quad (5)$$

These parameter vectors ε^{TOP} and ε^{ACT} are determined through regression analysis based on a set of training examples, which consist of bimetallic NP structures and their calculated energies (see Sec. II G). We use linear ridge regression as implemented in the scikit-learn Python package,[85] which introduces a regularization term in the normal equation for handling collinearities in the ACT and TOP descriptor spaces.

Note that only 88 of the 94 N^{ACT} descriptors in Eq. (3) are linearly independent for the 201-atom particle shown in Fig. 2. It is therefore necessary to add a regularization term to the linear regression, which allows both dealing with such linear dependencies in the

descriptor space and carrying out the regression with fewer than 88 data points (i.e., carrying out an underdetermined linear regression).

G. Constructing reference datasets

Training (or parameterizing) a surrogate energy model requires a reference dataset of NPs with various chemical orderings, containing their descriptors and calculated energies. In this work, we constructed datasets differing in the level of theory used to calculate the reference energy (DFT or EMT) for varying metals forming the nanoalloy. Namely, we constructed four reference datasets for $Pt_{201-x}Au_x$ and $Pt_{201-x}Cu_x$ NPs—two of them with the fixed stoichiometry ($Pt_{101}Au_{100}$ and $Pt_{101}Cu_{100}$) and the other two with variable stoichiometry $0 \le x \le 201$. Each of these datasets contains 1000 locally relaxed NP structures using the EMT potential. An additional reference dataset of 600 locally relaxed structures of the $Pd_{140-x}Zn_x$ NPs ($1 \le x \le 139$) was constructed using DFT.

To ensure structural diversity in our datasets, we first created much larger datasets of NP structures (without calculating their energy) and subsequently selected maximally differing points. Namely, these larger databases contain 8.5×10^6 and 2.5×10^6 structures for the 201-atom and 140-atom NPs, respectively. These large datasets were created by selecting snapshots of different runs of chemical ordering optimizations using a Monte Carlo algorithm with different combinations of arbitrary parameters. To identify a subset of maximally different structures for each system, we then used the Maximum Distance Sampling (MDS) algorithm,[85] sequentially identifying each new structure to be added to the subset, which has the largest Euclidean distance (in the space of ACT descriptors) to all structures already included in the subset.

H. Global optimization algorithms

In Sec. III, we demonstrate that surrogate energy models can achieve accuracy levels comparable to those of the theory used to construct the dataset, while requiring a much smaller computational cost. This makes these models particularly suited for their use in global optimization methods that algorithmically evaluate millions of candidate structures to find the lowest-energy one. In this study, we employed a recently developed Basin Hopping (BH) method combined with the optimal exchange algorithm[86] to optimize the chemical ordering of bimetallic NPs. This algorithm relies on approximations to the stability of each atom of the system to carry out deterministic local relaxations in the space of chemical ordering. Such local relaxations are thus carried out by selecting permutations between two atoms of different elements with the largest possible energy gains. After convergence of the optimal exchange relaxation to a basin in the space of chemical ordering, a number of perturbative permutations are carried out randomly to escape from the basin. This optimal exchange BH approach requires energy evaluation for an order of magnitude fewer candidate structures than Markov chain Monte Carlo and genetic algorithms.

The permutation between two atoms leading to maximal energy gain can be identified by calculating the local energy of every atom in the NP.[86] Within the surrogate energy model using the TOP or ACT descriptors, the local energy $F_s(n_{AA}, n_{AB})$ of an atom with element index s can be approximated by the number of homometallic (n_{AA}) and heterometallic (n_{AB}) bonds it forms with neighboring atoms. For an exemplary TOP descriptor,

$$F_s(n_{AA}, n_{AB}) = \varepsilon^{coor}_{n_{AA}+n_{AB}} + n_{AA}\varepsilon_{AA} + n_{AB}\varepsilon_{AB}, \tag{6}$$

where $\varepsilon^{coor}_{n_{AA}+n_{AB}}$, ε_{AA}, and ε_{AB} are the linear coefficients obtained from fitting Eq. (4) for $N^{coor}_{n_{AA}+n_{AB}}$, N_{AA}, and N_{AB}, respectively. For the ACT descriptor, $F_{s,n_{AA},n_{AB}}$ is instead equal to the coefficient $\varepsilon_{s,n_{AA},n_{AB}}$ for the corresponding s, n_{AA}, n_{AB} atom type,

$$F_s(n_{AA}, n_{AB}) = \varepsilon_{s,n_{AA},n_{AB}}. \tag{7}$$

To determine the most favorable targets for atom permutations, we calculate the flip energy E_i^{flip} for every atom of the NP as the difference in environment energies of the two elements in the same atomic environment,

$$E_i^{flip}(s_A, s_B) = F_1(n_{AA}, n_{AB}) - F_0(n_{AA}, n_{AB}). \tag{8}$$

When using the ACT descriptor, an extra $\sum_j^{\mathrm{N}} \Delta\varepsilon^j_{s,n_{AA},n_{AB}}$ term is added to Eq. (8) accounting for the change in the environment of every neighbor atom j. Equation (8) therefore represents the surrogate energy change associated with swapping the identity of the atom in the NP.

The optimal exchanges of atoms can be used to carry out deterministic relaxations in the chemical ordering space, converging to a local or global minimum, i.e., an ordering for which any permutation results in an energy increase. These local relaxations are alternated in a BH algorithm with perturbation phases consisting of several random permutations, which allow us to escape local minima. Both the number of relaxation–perturbation cycles and the number of random permutations per perturbation are tunable parameters in a BH algorithm. In the current work, we carry out up to 1000 relaxation–perturbation cycles, where in each perturbation cycle, seven random permutations are executed.

III. RESULTS AND DISCUSSION

In this work, we have evaluated the performance of surrogate energy models that quantify the energies of bimetallic NP structures with different chemical orderings. We first describe the performance of several TOP SEMs (Sec. III A) and analyze the corresponding ε^{TOP} coefficients, focusing on their interpretability. Section III B deals with the accuracy, data-efficiency, and transferability of TOP and ACT SEMs. Section III C illustrates the performance of these energy models for globally optimizing PtCu, PtAu, and PdZn nanoalloys of either fixed or variable stoichiometry.

A. Performance of TOP surrogate energy models

We begin by evaluating the performance of SEMs using different numbers and types of topological descriptors for quantifying the energy of bimetallic NPs. In particular, we compare the TOP SEMs: (a) accounting only for the number of heterometallic bonds N_{AB}; (b) accounting only for the number of homo- and heterometallic bonds (N_{AA} and N_{AB}); (c) a coordination-based model accounting only for the number of occurrences of element A in different positions ($N_{\mathrm{A},6}$, $N_{\mathrm{A},7}$, $N_{\mathrm{A},8}$, $N_{\mathrm{A},9}$); (d) the TOP SEM as originally formulated by Kozlov *et al.*,[49] which accounts for the number of heterometallic bonds and the number of atoms of one of the two elements in surface positions with different coordination numbers (N_{AB}, $N_{\mathrm{A},6}$, $N_{\mathrm{A},7}$,

$N_{A,8}$, and $N_{A,9}$); (e) a model including the largest possible number of linearly independent descriptors (N_{AA}, N_{AB}, $N_{A,6}$, $N_{A,7}$, $N_{A,8}$, and $N_{A,9}$); and (f) a model including all topological descriptors, despite some being linearly correlated (N_{AA}, N_{AB}, N_{BB}, $N_{A,6}$, $N_{A,7}$, $N_{A,8}$, $N_{A,9}$, $N_{A,12}$, $N_{B,6}$, $N_{B,7}$, $N_{B,8}$, $N_{B,9}$, and $N_{B,12}$). We evaluate the performance of these SEMs for describing the energies within one set of single stoichiometry $Pt_{100}Au_{101}$ homotops and one set of variable stoichiometry $Pt_{201-x}Au_x$ (x = 1–200) homotops.

1. Stoichiometry $Pt_{100}Au_{101}$

The TOP models mentioned above were trained and evaluated on a single-stoichiometry dataset of 1000 homotops of $Pt_{100}Au_{101}$ NPs featuring the *fcc* crystal structure. The atomic positions in these homotops were relaxed at the EMT level of theory, so the energies used for training correspond to those of the local minima of the potential energy surface. The 1000 structures were retrieved from our database using the MDS algorithm (see Sec. II G). Since the TOP-SEMs converge with a small number of training structures, we used up to 100 homotops for training and the remaining 900 homotops for testing. The resulting learning curves in Fig. 4 show the evolution of the distribution of Mean Absolute Error (MAE) over 100 cross-validation splits. The solid lines correspond to the median MAE, and the shaded areas indicate the first and third quartiles of the error distribution.

The median MAE for the simplest model accounting just for the number of heterometallic bonds is quite large [8.0 meV/atom, Fig. 4(a)], but reasonably good for a one-dimensional descriptor. This indicates that accounting for the degree of metal mixing (more AB bonds correspond to more mixed structures) is a good first descriptor of homotop stability. Indeed, data on the miscibility of metals, closely related to the preference of forming heterometallic bonds between atoms of these metals, are widely used in the practical assessment of the ordering patterns of metal alloy particles.[1] Adding N_{AA} to produce a bond-centered model significantly reduces the MAE values to 1.0 meV/atom [Fig. 4(b)], which is smaller than half of that obtained for the coordination-based model [2.3 meV/atom, Fig. 4(c)]. This indicates that the nature of the bonds that each atom forms carries more information than the coordination number of the atom. This is unsurprising, given that one can infer the coordination number of an atom by the number of homometallic and heterometallic bonds it forms, but not the other way around. Combining the bond-centered and coordination-centered descriptors (giving rise to, among others, the originally formulated TOP descriptor vector) yields even lower errors, with MAE values of 0.6 meV/atom [see Figs. 4(d)–4(f)]. We note that the TOP model as formulated in Ref. 49 is only missing the N_{AA} variable (or N_{BB}, which is an equivalent addition due to the fixed by the NP morphology number of all bonds) to contain a maximal number of linearly independent TOP descriptors (for a fixed stoichiometry). Adding of the N_{AA} term, however, only leads to a marginal improvement in the errors for the $Pt_{100}Au_{101}$ dataset [Fig. 4(e)]. Adding further descriptors that are linearly dependent expectedly does not change the MAE values at all [Fig. 4(f)].

The data efficiency, understood as the number of training points required to reach the convergence of the SEM parameters, also depends on the set of descriptors chosen. Here, we consider a model converged when increasing the number of training examples results in an improvement of less than 0.05 meV in the median MAE. The coordination-based model converges at ~60 training examples, whereas bond-centered and combined models do so with fewer than

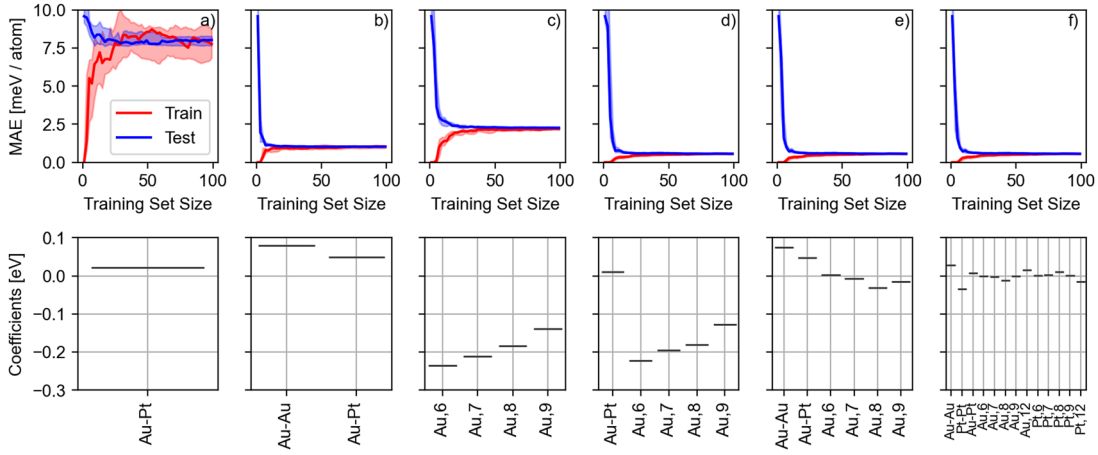

FIG. 4. Learning curves (top row) and regression coefficients (bottom row) obtained with models using different sets of topological descriptors to represent a single-stoichiometry $Pt_{100}Au_{101}$ NP homotops: (a) a bond-centric model accounting only for the number of heterometallic bonds (N_{AuPt}); (b) a bond-centric model accounting for the number of both heterometallic (N_{AuPt}) and homometallic (N_{AuAu}) bonds; (c) a model based on coordination numbers (CNs) accounting only for the number of occurrences of one of the two elements in positions with different CNs ($N_{Au,6}$, $N_{Au,7}$, $N_{Au,8}$, $N_{Au,9}$); (d) the TOP model as originally formulated[49] accounting for the number of heterometallic bonds and coordination numbers of surface atoms (N_{AuPt}, $N_{Au,6}$, $N_{Au,7}$, $N_{Au,8}$, $N_{Au,9}$); (e) a model including the maximum number of possible linearly independent descriptors (N_{AuAu}, N_{AuPt}, $N_{Au,6}$, $N_{Au,7}$, $N_{Au,8}$, $N_{Au,9}$), i.e., adding N_{AuAu} to model (d); and (f) a model including all descriptors, despite some being linearly dependent (N_{AuAu}, N_{AuPt}, N_{PtPt}, $N_{Au,12}$, $N_{Au,9}$, $N_{Au,8}$, $N_{Au,7}$, $N_{Au,6}$, $N_{Pt,12}$, $N_{Pt,9}$, $N_{Pt,8}$, $N_{Pt,7}$, $N_{Pt,6}$). The blue and red lines in the learning curves correspond to the median testing and training errors, respectively, resulting from 100 cross-validation splits. The shaded areas indicate the error distribution within the first and third quartiles. A version of these plots in logarithmic scale is shown in Fig. S2.

25 training examples. This is a particular advantage of TOP-SEMs, which achieve accuracies of ~0.5 meV/atom while training with just 24 structures.

We next focus on the values of the coefficients ε^{TOP} resulting from the linear regression. In previous studies,[50–59] such coefficient values have been analyzed to evaluate the preference of a particular nanoalloy to form homometallic or heterometallic bonds, or to expose atoms of one element in positions with a given coordination number. For example, a negative ε_{AB} value often correlates with a preference to form heterometallic bonds compared to homometallic ones, whereas a negative value of $\varepsilon^{coor}_{A,CN}$ often points to preference of element A to occupy the CN-coordinated position with respect to element B doing so, provided that all other descriptors remain the same. Such an approximate decomposition of the interaction energy has been satisfactorily carried out with the TOP model for different nanoalloy systems (as originally formulated with only ε_{AB} and $\varepsilon^{coor}_{A,CN}$ coefficients).[50–59]

For the $Pt_{101}Au_{100}$ nanoalloy, the original TOP model [considering N_{AuPt}, $N_{Au,6}$, $N_{Au,7}$, $N_{Au,8}$, and $N_{Au,9}$, see Fig. 4(d)] leads to positive ε_{AuPt} and to negative $\varepsilon^{coor}_{Au,6}$, $\varepsilon^{coor}_{Au,7}$, $\varepsilon^{coor}_{Au,8}$, and $\varepsilon^{coor}_{Au,9}$, with the coordination terms decreasing in magnitude with increasing CN.[87] The positive ε_{AuPt} coefficient is consistent with the preference in such particles to separate the Au and Pt atoms into shell and core regions, respectively, which exhibit fewer heterometallic bonds than well-mixed homotops. The preferred Pt-core, Au-shell arrangement is also consistent with the negative $\varepsilon^{coor}_{Au,6}$, $\varepsilon^{coor}_{Au,7}$, $\varepsilon^{coor}_{Au,8}$, and $\varepsilon^{coor}_{Au,9}$ coefficients, which indicate that placing a Pt atom in one of these positions increases the energy. In addition, the variation of the coordination coefficients indicates that Au preferably occupies lower-coordinated sites, in line with observed global minima orderings found for PtAu nanoalloys.

This seemingly robust interpretability of the regression coefficients for the $Pt_{101}Au_{100}$ nanoalloy is less straightforward for more complex models (as shown below) or for nanoalloys with more complex bulk orderings. Both the magnitude and sign of the ε^{TOP} terms are in fact dependent on which descriptors are included in the model. In particular, the order in magnitude of the $\varepsilon^{coor}_{Au,CN}$ coefficients of the coordination-based model is preserved when adding N_{AuPt}, but the further addition of the N_{AuAu} descriptor to the model inverts the order from $\varepsilon^{coor}_{Au,6}$ to $\varepsilon^{coor}_{Au,9}$, even resulting in a positive $\varepsilon^{coor}_{Au,6}$. In turn, the coefficients ε_{AuPt} and ε_{AuAu} seem to preserve their sign and relative magnitudes across all models where both N_{AuPt} and N_{AuAu} are included. Does that mean that the two models (with and without N_{AuAu}) exhibit a different preference for Au to occupy 6-coordinated positions? Both the similar accuracy and the minimum energy homotops obtained during global optimization using the two models indicate otherwise. The change in ε^{TOP} values therefore reflects that increasing the complexity of a model by increasing the number of interrelated parameters in general makes the model coefficients harder or sometimes just impossible to interpret. This is then related to the fact that the number of bonds and coordination number are not completely independent from one another (albeit not explicitly linearly correlated). This is more clearly illustrated by the massive effect on the coefficients of adding linearly correlated descriptors, even when using regularization [see Fig. 4(f)], despite not altering the accuracy of the model.

2. Variable stoichiometry $Pt_{201-x}Au_x$ (x = 1–200)

The same six TOP-SEMs were trained and evaluated on a multiple-stoichiometry dataset of 1000 homotops of $Pt_{201-x}Au_x$ NPs, created using the same strategy as the single-stoichiometry one. However, to account for changes in composition, the number of Au

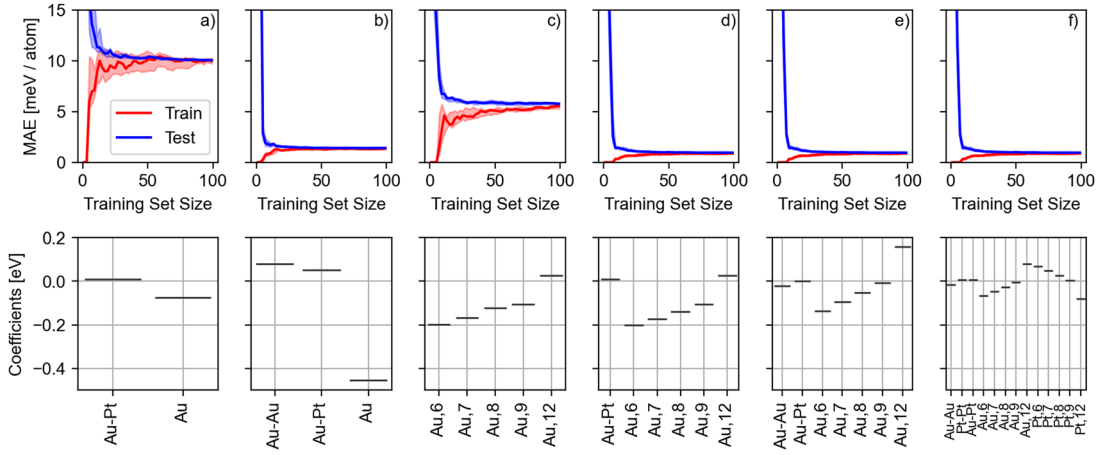

FIG. 5. Learning curves (top row) and regression coefficients (bottom row) obtained with models using different sets of topological descriptors to represent variable stoichiometry $Pt_{201-x}Au_x$ NP homotops (x = 1–200): (a) A bond-centric model accounting for the number of heterometallic bonds and the number of Au atoms (N_{AuPt}, N_{Au}); (b) a bond-centric model accounting for the number of homo- and heterometallic bonds and the number of Au atoms (N_{AuAu}, N_{AuPt}, N_{Au}); (c) a model based on coordination numbers (CNs) accounting only for the number of occurrences of one of the two elements in positions with different CNs ($N_{Au,6}$, $N_{Au,7}$, $N_{Au,8}$, $N_{Au,9}$, $N_{Au,12}$); (d) the TOP model as originally formulated[49] accounting for the number of heterometallic bonds and the number of occurrences of one of the two elements in surface and bulk positions with different coordination numbers (N_{AuPt}, $N_{Au,6}$, $N_{Au,7}$, $N_{Au,8}$, $N_{Au,9}$, $N_{Au,12}$); (e) a model including all linearly independent descriptors (N_{AuAu}, N_{AuPt}, $N_{Au,6}$, $N_{Au,7}$, $N_{Au,8}$, $N_{Au,9}$, $N_{Au,12}$); and (f) a model including all descriptors, despite some being linearly correlated (N_{AuAu}, N_{AuPt}, N_{PtPt}, $N_{Au,12}$, $N_{Au,9}$, $N_{Au,8}$, $N_{Au,7}$, $N_{Au,6}$, $N_{Pt,12}$, $N_{Pt,9}$, $N_{Pt,8}$, $N_{Pt,7}$, $N_{Pt,6}$). The blue and red lines in the learning curves correspond to the median testing and training errors, respectively, resulting from 100 cross-validation splits. The shaded areas indicate the error distribution within the first and third quartiles. A version of these plots in logarithmic scale is shown in Fig. S3.

atoms (N_{Au}) was added as a descriptor to the bond-centric models [Figs. 5(a) and 5(b)] and the number of 12-coordinated Au atoms ($N_{Au,12}$) was added to the coordination-based model [Fig. 5(c)] and to the original TOP formulation [Fig. 5(d)].

The errors for each of the converged models are larger than for the single-stoichiometry set, with median MAE values of 10.1, 1.4, and 5.8 meV/atom for the heterometallic bond-centric (N_{AuPt}, N_{Au}), bond-centric (N_{AuAu}, N_{AuPt}, N_{Au}), and coordination-based ($N_{Au,6}$, $N_{Au,7}$, $N_{Au,8}$, $N_{Au,9}$, $N_{Au,12}$) models, respectively, and 1.0 meV/atom for the original TOP model with added $N_{Au,12}$ (N_{AuPt}, $N_{Au,6}$, $N_{Au,7}$, $N_{Au,8}$, $N_{Au,9}$, $N_{Au,12}$), the model with all linearly independent descriptors (N_{AuAu}, N_{AuPt}, $N_{Au,6}$, $N_{Au,7}$, $N_{Au,8}$, $N_{Au,9}$, $N_{Au,12}$), and the model with all descriptors (N_{AuAu}, N_{AuPt}, N_{PtPt}, $N_{Au,12}$, $N_{Au,9}$, $N_{Au,8}$, $N_{Au,7}$, $N_{Au,6}$, $N_{Pt,12}$, $N_{Pt,9}$, $N_{Pt,8}$, $N_{Pt,7}$, $N_{Pt,6}$). The errors for the best models are therefore approximately twice as large when predicting the relative stability of homotops in the variable-stoichiometry set than in the single-stoichiometry case.

The regression coefficients are, in turn, also generally interpretable, with positive ε_{AuPt} and $\varepsilon^{coor}_{Au,CN}$ values that decrease in magnitude with increasing CN. In addition, $\varepsilon^{coor}_{Au,12}$ is positive for almost all models, reflecting the strong preference of Pt to occupy 12-coordinated positions. We note that for the model including all descriptors, $\varepsilon^{coor}_{Pt,CN}$ coefficients follow an opposite trend to $\varepsilon^{coor}_{Au,CN}$ ones, with $\varepsilon^{coor}_{Au,CN} \equiv -\varepsilon^{coor}_{Pt,CN}$, consistent with the higher energy costs of placing Pt in less coordinated positions. The interpretation of $\varepsilon^{coor}_{Au,CN}$ coefficients seems therefore more robust for the variable stoichiometry set than for the single-stoichiometry one.

B. Accuracy and data-efficiency of TOP-SEM vs ACT-SEM

After establishing the accuracy of different TOP models and analyzing the resulting coefficients, we compare the best performing TOP model against the ACT model described in Sec. II E. Each model is tested on three different nanoalloy systems exhibiting different most-stable orderings, i.e., PtAu (core–shell), PtCu (well-mixed), and PdZn (layered). We evaluate the performance in terms of the accuracy of the energy predictions (MAE), the data-efficiency (number of required training examples), and the transferability (across varying stoichiometries). We also compare the energy of their predicted global-minimum structure, as well as the number of global optimization steps required to reach such minimum (the cumulative success rate of the GO algorithm).

1. $Pt_{101}Au_{100}$ and $Pt_{101}Cu_{100}$ nanoparticles

The learning curves obtained when training and testing with $Pt_{101}Au_{100}$ and $Pt_{101}Cu_{100}$ NPs are shown in Figs. 6(a) and 6(c). The models are evaluated using 100 cross-validation splits, dividing the dataset into 500 training homotops plus 500 testing homotops. The MAE of the converged models reveals that (i) errors are larger for $Pt_{101}Cu_{100}$ than for $Pt_{101}Au_{100}$, (ii) ACT models are more accurate than TOP models, and (iii) TOP models are more data-efficient (i.e., they converge with fewer training examples). In particular, the MAE for $Pt_{101}Au_{100}$ and $Pt_{101}Cu_{100}$ is 0.5 and 1.6 meV/atom, respectively, with the TOP model, and 0.2 and 0.5 meV/atom, respectively, with the ACT model. The ACT model is therefore approximately three times more accurate than the TOP model, but this comes at the cost of requiring significantly more training examples to parameterize. TOP models for $Pt_{101}Au_{100}$ and $Pt_{101}Cu_{100}$ nanoalloys are converged after 31 and 141 training examples, respectively, while ACT models required 201 and 301 training examples, respectively. A model is considered converged when adding a new training example does not improve the test-set MAE by > 0.01 meV/atom.

The higher accuracy and data requirements of the ACT model are due to higher dimensions of ACT descriptors compared to TOP ones. The six coefficients of the ε^{TOP} vector can be parameterized with a small number of training structures, but this limited dimension does not allow us to further learn from larger training sets. Instead, reliably parameterizing the 94 coefficients of the ε^{ACE} vector by linear regression would require at least 94 training examples with linearly independent $\boldsymbol{N}^{ACT}$ descriptors. We recall that only 88 of the 94 descriptors in $\boldsymbol{N}^{ACT}$ are linearly independent for the 201-atom particle shown in Fig. 2. It is therefore necessary to add a regularization term to the linear regression, which allows dealing with such linear dependencies in the descriptor space and training with fewer than 88 training examples (i.e., carrying out underdetermined linear regression).

The lower accuracy calculated for the PtCu nanoalloy is partially due to a stronger interaction between Pt and Cu than between

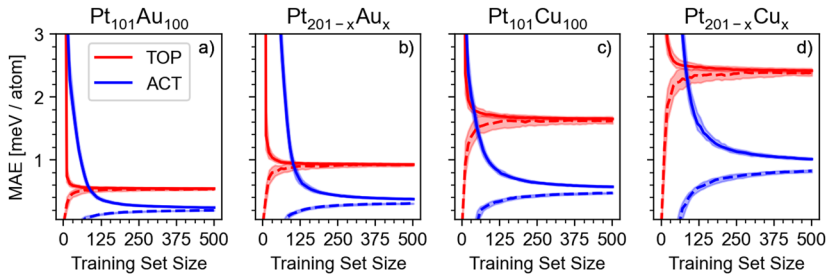

FIG. 6. Learning curves obtained from models using the TOP (red lines) and ACT (blue lines) descriptors to approximate the energies of PtAu and PtCu homotops. The TOP model includes the descriptors N_{AA}, N_{AB}, $N_{A,6}$, $N_{A,7}$, $N_{A,8}$, and $N_{A,9}$. (a) and (b) Learning curves obtained using a database of 1000 EMT energies of $Pt_{101}Au_{100}$ and $Pt_{201-x}Au_x$ (x = 1–200) truncated octahedral NPs. (c) and (d) Learning curves obtained using a database of 1000 EMT energies of $Pt_{101}Cu_{100}$ and $Pt_{201-x}Cu_x$ (x = 1–200) truncated octahedral NPs. Panels (a) and (c), therefore, correspond to particles with 1:1 stoichiometry only, whereas panels (b) and (d) correspond to particles with varying stoichiometry. Each of the 1000-NP datasets was split into training and testing sets of 500 points each. Continuous and dashed lines correspond to the median testing and training errors, respectively. The shaded areas indicate the error distribution within the first and third quartiles resulting from 100 cross-validation splits.

Pt and Au and due to a larger mismatch between the lattice parameters of Pt and Cu than of Pt and Au. Such a larger mismatch leads to more distorted relaxed structures. This affects the accuracy, because both ACT and TOP models are trained on relaxed structures, but their descriptors are identical for relaxed and unrelaxed systems (i.e., they do not capture structural changes induced by local relaxation). Training on the energies of unrelaxed structures could therefore improve the accuracy of the models but would miss any relaxation-induced stabilization of particular orderings.

2. $Pt_{201-x}Au_x$ and $Pt_{201-x}Cu_x$ nanoparticles ($x = 1$–200)

The learning curves obtained when training and testing with datasets of variable stoichiometry [Figs. 6(b) and 6(d)] exhibit larger errors than their single stoichiometry counterparts. These datasets were constructed by selecting subsets of 1000 NPs from the large database by means of the MDS algorithm. Larger MAE values obtained for these subsets with respect to the single stoichiometry case were expected due to the increased diversity of the multiple stoichiometry sets. However, the error increase is more significant for the TOP model, with MAE values going from 0.5 to 0.9 meV/atom for the $Pt_{201-x}Au_x$ NPs and from 1.6 to 2.4 meV/atom for the $Pt_{201-x}Cu_x$ NPs. In turn, for the ACT models, the MAE values go from 0.2 to 0.4 meV/atom for the $Pt_{201-x}Au_x$ NPs and from 0.6 to 1.1 meV/atom for the $Pt_{201-x}Cu_x$ NPs. Errors of the ACT and TOP models are therefore doubled for multiple stoichiometry datasets compared to single stoichiometry ones. The multiple stoichiometry models also require more training points (e.g., 421 for $Pt_{201-x}Au_x$ and 461 for $Pt_{201-x}Cu_x$) for obtaining converged ACT models (with MAE variations <0.05 meV upon adding a new training structure), making them less data-efficient than the single stoichiometry counterparts, albeit being able to describe much larger spaces of chemical ordering. Note that the prediction errors of the ACT model are lower than those of the TOP models when using 91, 51, 111, and 91 training structures for the $Pt_{101}Au_{100}$, $Pt_{101}Cu_{100}$, $Pt_{201-x}Au_x$, and $Pt_{201-x}Cu_x$ NPs, respectively. Thus, a better data-efficiency of the TOP model is only an advantage when dealing with quite small datasets.

We next evaluate the model errors as a function of training and testing stoichiometry. Figure 7 illustrates the evolution, with the size of the variable stoichiometry training set, of the predicted $Pt_{201-x}Au_x$ and $Pt_{201-x}Cu_x$ NP energies as a function of the testing stoichiometry for TOP and ACT models. As already seen in Fig. 6, ACT models require more training structures to converge, but achieve lower errors. In particular, TOP models are only marginally improved upon training set size increase beyond 50 structures, whereas the ACT models keep improving until up to 200 and 500 training examples for the PtAu and PtCu NPs, respectively. In addition, Fig. 7 reveals that errors for the TOP models are quite unevenly distributed, with particularly large errors for stoichiometries with low concentrations of one of the two metals. The MAE values decrease steeply starting from the single-metal stoichiometries, reaching a minimum for $x \approx 20$–25 and for $x \approx 170$. The TOP errors for intermediate stoichiometries (i.e., from 1:4 to 4:1) are rather uniform and lie at ~1 and 2 meV/atom for $Pt_{201-x}Au_x$ and $Pt_{201-x}Cu_x$ NP energies. This indicates that the TOP models are quite accurate and stable for the 1:3, 1:1, and 3:1 stoichiometries often addressed in previous studies.[50–59] The errors for the ACT models are very differently distributed across stoichiometries compared to the TOP models, with larger ACT MAE values at intermediate stoichiometries than at low concentrations of one of the two metals. The errors are, however, significantly lower than for the TOP model, even for stoichiometries in which TOP models perform best.

To further evaluate the transferability of the TOP and ACT models, we calculated the errors obtained when training and testing with different single-stoichiometry sets (see Fig. S1). As expected, the lowest errors are obtained when training and testing sets have similar or equal stoichiometry. In addition, errors of the TOP models are, in general, much lower than those of ACT models, remaining <5 meV/atom for almost all combinations of learning and

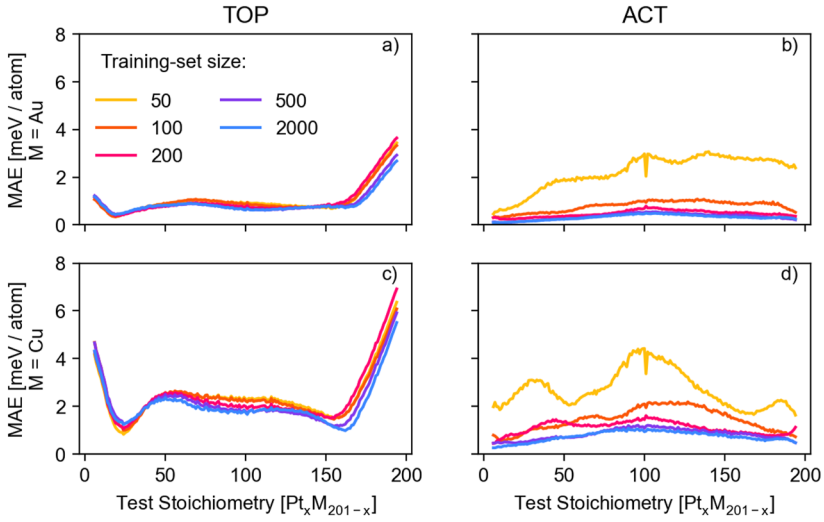

FIG. 7. Mean absolute errors (MAEs) of the predicted $Pt_{201-x}Au_x$ (a) and (b) and $Pt_{201-x}Cu_x$ (c) and (d) NP energies as a function of the testing stoichiometry for TOP (a) and (c) and ACT (b) and (d) models trained with variable stoichiometry datasets of different sizes (i.e., with 50, 100, 200, 500, and 2000 training examples as coded by colors).

testing stoichiometry. Errors for the ACT models are particularly large when training and testing with very different stoichiometries, which leads to MAE values up to ~50 meV/atom. These large errors appear because NPs with very different metal contents often exhibit different sets of atom-types. This means that structures included in the test set contain atom-types that the model has not encountered in the training set. We should highlight that obtaining a given $\varepsilon_{x,aa,bb}$ when training with a dataset in which $N_{x,aa,bb}$ is zero for all training structures is only possible technically (albeit ill-advised) because of the regularization applied when carrying out linear regression. In any case, it is simpler to select a training set that includes non-zero values for all feature vector elements when using the ACT descriptors. TOP models are correspondingly more transferable, and one could train with a dataset made of NPs with 1:1 stoichiometry to obtain accurate enough predictions for NPs with 1:3 to 3:1 stoichiometry. We reiterate, however, that training with variable-stoichiometry datasets yields lower errors for variable stoichiometry test sets.

C. Performance of global optimization approaches based on TOP and ACT SEMs

1. $Pt_{101}Au_{100}$ and $Pt_{101}Cu_{100}$ nanoparticles

After evaluating the accuracy of the TOP and ACT surrogate energy models, we focus on their adequacy when used in global optimization algorithms of the chemical ordering of bimetallic NPs. We evaluated the quality of the minimum-energy structures obtained with each model and the rate at which the algorithm can successfully identify such global minima. Figure 8 illustrates the evolution of the cumulative success rates with the number of evaluated structures when using the basin hopping algorithm described in Sec. II H for globally optimizing the chemical ordering of $Pt_{101}Au_{100}$ and $Pt_{101}Cu_{100}$ NPs, evaluating the energy of each candidate with either the TOP or ACT model. Cumulative success rates are obtained by initializing the GO search 100 independent times and tracking what percentage of such runs have found the global minimum (according to the SEM used within the algorithm) as a function of the number of evaluated structures.

The cumulative success rates shown in Figs. 8(a) and 8(b) indicate that the BH algorithm requires evaluating ~3 orders of magnitude more candidate NP structures for PtCu than for PtAu nanoalloys. The relative performance of GO algorithms combined with either TOP or ACT energy models is, surprisingly, system dependent. In particular, the TOP model yields more successful optimizations of the chemical ordering of PtAu NPs than the ACT model, whereas optimizations with the ACT model are more successful for the PtCu NPs. This is probably related to the fact that the global minima for PtAu NPs exhibit a core–shell structure with Au atoms occupying surface positions and that the TOP model is particularly suited for predicting preferred positions of the two metals at the surface of the NP. The better performance of the ACT model for the global optimization of PtCu is, in turn, probably due to the higher sensitivity of the ACT descriptor to different arrangements in the inner regions of the NP, which is more relevant for well-mixed bimetallic alloys like PtCu.

Comparing the EMT energies of the identified minima for each of the four cases illustrated in Figs. 8(c)–8(e), we find that the BH algorithm combined with the ACT model finds slightly

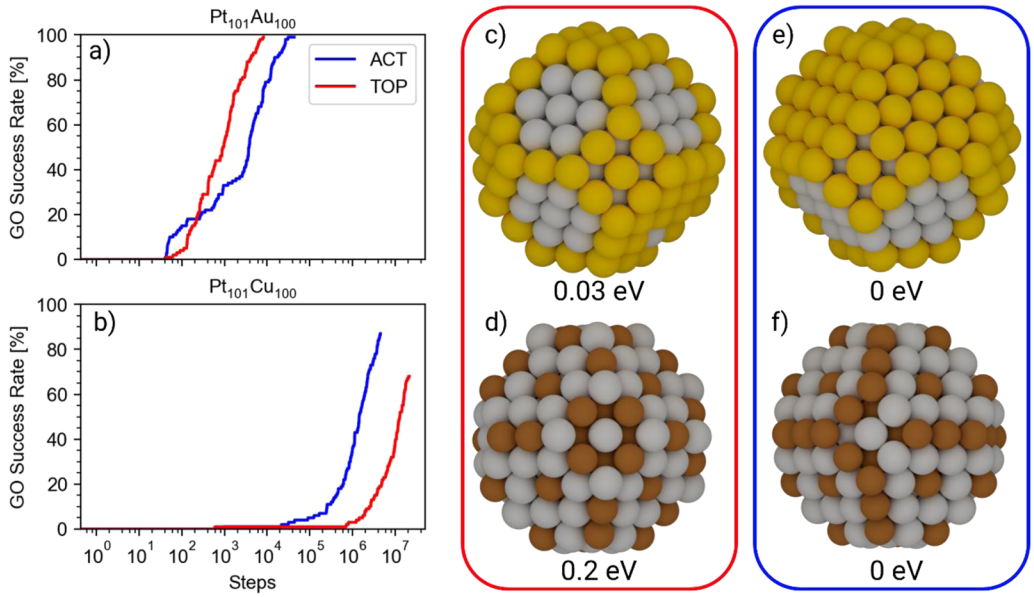

FIG. 8. Cumulative success rate as a function of the number of evaluated structures of 100 global optimization runs using a basin hopping approach for (a) $Pt_{101}Au_{100}$ and (b) $Pt_{101}Cu_{100}$. The red and blue lines correspond to cumulative success rates obtained using the TOP and ACT energy models, respectively. Success is here defined as finding the lowest-energy structure according to each surrogate energy model. In red and blue frames are the lowest-energy orderings for the $Pt_{101}Au_{100}$ (upper images) and $Pt_{101}Cu_{100}$ (lower images) NPs obtained from global optimization using the TOP (c) and (d) and ACT (e) and (f) energy models, respectively. The numbers below the NP images are the EMT energies relative to the EMT energy of the putative global minimum.

better-quality (more stable) structures than when combined with the TOP model. Thus, despite the better data-efficiency and (in some cases) better success rate of the BH+TOP approach, the BH+ACT approach finds structures that are closer to the EMT global minimum (if not exactly it).

2. $Pd_{140-x}Zn_x$ (x = 1–139) nanoparticles

In Secs. II A and II B, we have evaluated the accuracy of the TOP and ACT energy models for reproducing reference PtAu and PtCu nanoalloy energies calculated with EMT. To examine whether the TOP and ACT approaches can also describe nanoalloys calculated at different levels of theory, we trained both models on a dataset of $Pd_{140-x}Zn_x$ NPs structures with variable stoichiometry calculated by DFT (see computational details in Sec. II A).

Pd and Zn form nanoalloys, with strong intermetallic bonds and significant exchange of charge between Pd and Zn.[49] This strong interaction results in stable layered $L1_0$ chemical ordering with alternated Pd and Zn layers in the [100], [010], or [001] directions of the fcc lattice.[88] The perfectly layered chemical orderings of PdZn NPs are stable in part because they enable a significant relaxation, which distorts the NP shape by contracting in the direction perpendicular to the layers and expanding in the directions parallel to the layers. This pronounced stabilization by relaxation upon acquiring layered orderings makes an accurate representation challenging for the TOP and ACT models, which rely on the in-lattice approximation and therefore cannot explicitly account for relaxations undergone by different chemical orderings. The TOP model is also not well suited for differentiating layered structures. Kozlov *et al.* partially remediated this limitation by adding a term in the TOP model representing how close each layer in a given direction (i.e., the [100]) is to being homometallic.[49] The *ad hoc* term, however, considers layers only in one direction and disregards whether layers are formed in any of the other two orthogonal directions.

To establish the performance of the TOP and ACT models for these challenging intermetallic alloys, we trained both models with a dataset of 600 Pd_xZn_{140-x} (x = 1–139) NP structures and their DFT energies. This dataset includes layered orderings to partially account for this particularly stable region of the chemical ordering space. The dataset was split into 400 training and 200 testing examples in different cross-validation splits. Learning curves in Fig. 9(a) show that the ACT model is more accurate than the TOP model, with converged MAE values of 7.7 and 18.1 meV/atom, respectively. As was the case for learning EMT energies of PtAu and PtCu NPs, the TOP model converges with much fewer reference structures (~50) than the ACT model (~300). However, the ACT model performs better (i.e., with lower MAE values) than the TOP model already for training sets larger than 90.

To evaluate the performance of the two SEMs during global optimization of the chemical ordering, we retrained the ACT and TOP models with all structures of the database and use the resulting energy expressions in combination with the BH algorithm. There

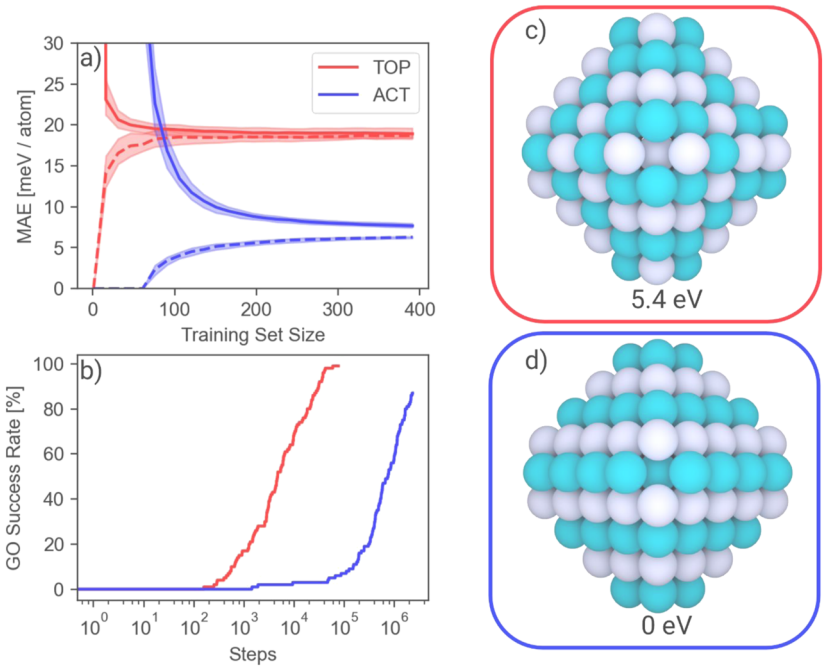

FIG. 9. Performance of ACT and TOP models for $Pd_{140-x}Zn_x$ nanoalloys. (a) Learning curves of the TOP (red) and ACT (blue) energy models obtained for a dataset of 600 $Pd_{140-x}Zn_x$ structures and their DFT energies. (b) Cumulative success rate of the BH algorithm in finding the lowest-energy chemical ordering of the $Pd_{72}Zn_{68}$ NP during 100 GO runs with the TOP (red) or ACT (blue) energy models. (c) Lowest-energy ordering for the $Pd_{72}Zn_{68}$ NP obtained from global optimization with the TOP energy model. (d) Lowest-energy ordering for the $Pd_{72}Zn_{68}$ NP obtained from global optimization with the ACT energy model. Relative DFT energies of these lowest-energy orderings are shown in the bottom of panels (c) and (d).

is a three orders of magnitude difference in the number of candidate structures that the BH algorithm needs to evaluate to find the minimum-energy structure according to each SEM, with the BH+TOP requiring fewer candidate evaluations [Fig. 9(b)]. However, the BH algorithm with the TOP model converges to a structure that, despite being the global minimum for the $Pd_{72}Zn_{68}$ stoichiometry according to the TOP model [Fig. 9(c)], notably differs from the structure with the lowest DFT energy. In contrast, the BH runs with the ACT model converge to the perfectly layered structure, which is the minimum-energy ordering for both DFT and the ACT model [Fig. 9(d)]. Note, however, that the perfectly layered structure has the same ACT descriptor and therefore the same ACT energy as five other homotops, showing non-uniqueness of descriptor even in the more complex ACT SEM. These homotops are very similar to, but less stable at the DFT level than, the perfectly layered structure and result from permutations of Pd and Zn atoms in corner positions. The structure with perfectly layered ordering is 1–4 eV more stable than the other five structures with the same ACT descriptor. This is due to a very stabilizing relaxation that perfectly layered particles undergo, which is hard to capture unless these perfectly layered structures are included in the training set. In fact, BH runs with ACT models trained without such layered structures sometimes fail to converge to the most stable layered ordering. This points to the need to train the SEMs with NP structures near or at the region of chemical ordering space of the global minimum. However, since the global minimum is typically not known *a priori*, this calls for active learning approaches, where the model is iteratively retrained with relevant data points emerging from consecutive global optimization runs. This corresponds to the originally formulated TOP approach[49] and to more recent machine-learning assisted global optimization algorithms.[89,90]

3. Convex hull of $Pd_{140-x}Zn_x$ (x = 1–139) nanoparticles

With a surrogate energy ACT and TOP models able to describe the energies of all stoichiometries of the $Pd_{140-x}Zn_x$ NP, we optimized the chemical ordering for every stoichiometry to analyze the evolution of the structure as a function of Pd loading. Here, we also carried out two active learning cycles after the initial training and global optimization. In each cycle, the DFT energy of the putative global minimum (for both models) was calculated for 15 selected stoichiometries, the models were retrained with these new data points, and the optimization was restarted using these retrained models.

Relative stability of different compositions of a bimetallic NP can be compared by using the calculated mixing energy for the putative global minimum at every composition[91] as

$$E_{mix} = E_{Pd_nZn_m} - \frac{nE_{Pd_{140}} + mE_{Zn_{140}}}{(n+m)}, \tag{9}$$

where $E_{Pd_nZn_m}$ is the predicted energy of the nanoparticle global minimum found at that stoichiometry, n is the number of Pd atoms, and m is the number of Zn atoms in the NP. $E_{Pd_{140}}$ and $E_{Zn_{140}}$ are the reference energies of the homometallic NPs calculated with the same energy model as the bimetallic NPs. The E_{mix} calculated per atom as $E_{mix}/(n+m)$ allows us to evaluate the so-called convex hull of the nanoalloy.

To illustrate the quality of the predicted global minima, we plot the DFT mixing energies of the putative global minimum homotops

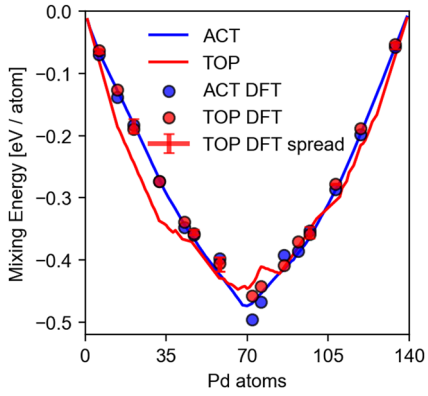

FIG. 10. Convex hull of $Pd_{140-x}Zn_x$ NPs obtained using the TOP and ACT models to determine the lowest-energy chemical ordering. The blue and red lines represent the mixing energy estimated with the TOP and ACT, respectively, of the corresponding global minima at varying NPs stoichiometries. The red and blue circles are DFT mixing energies for TOP and ACT global minima, respectively. Red error bars are used instead of red circles to indicate the spread in DFT mixing energy for stoichiometries for which the TOP feature vector of the TOP global minimum corresponds to various ACT feature vectors. Multimedia available online.

obtained by the two models for the 15 selected stoichiometries (see the red and blue points in Fig. 10). In general, the calculated DFT energies (mixing energies) are closer to the model-predicted ones for ACT than for TOP, with an average MAE of 11.140 (0.009) and 31.397 (0.027) meV/atom, respectively. Despite the better accuracy of the ACT SEM, in 4 out of 15 stoichiometries, the global minimum found by TOP had (by 1.027 for $Pd_{21}Zn_{119}$, 0.953 for $Pd_{58}Zn_{82}$, 2.168 for $Pd_{86}Zn_{54}$, and 0.623 for $Pd_{97}Zn_{43}$ eV) lower DFT energy than that found by ACT for the same stoichiometry.

Given the overall better accuracy of the ACT SEM, the lower energy of TOP-found minima with respect to ACT in these three cases is unlikely due to an intrinsic better energy description by the TOP SEM. Instead, for some stoichiometries, the larger errors of the TOP model and the more significant non-uniqueness of the TOP descriptors compared to the ACT ones give rise to a larger number of homotops with different ordering and wider range of DFT energies, but the same TOP descriptor and TOP energy. We have evaluated the presence of such inequivalent structures and calculated the spread in DFT energy (see the red error bars in Fig. 10). In many cases, the large spread in DFT energies of the TOP minima overlaps with the DFT energy of the ACT minima, indicating that the lower energies of the chemical orderings optimized with the TOP model are often obtained serendipitously.

Incomplete representations in the ACT training set of atom types found in the global minima could also lead to poor predictions with the ACT model. However, we have evaluated the abundance of all possible ACT atom types in the training set and analyzed which atom types comprise the global minima (see Fig. S4). The $Pd_{140-x}Zn_x$ NP training set covers all possible atom types, somewhat underrepresenting those with high fractions of heterometallic bonds. This is due to the fact that atom types with high fractions of heterometallic bonds are mostly present in diluted mixtures of the two metals, for which a relatively low number of homotops are possible (and therefore less frequently found in the training set). In addition, the

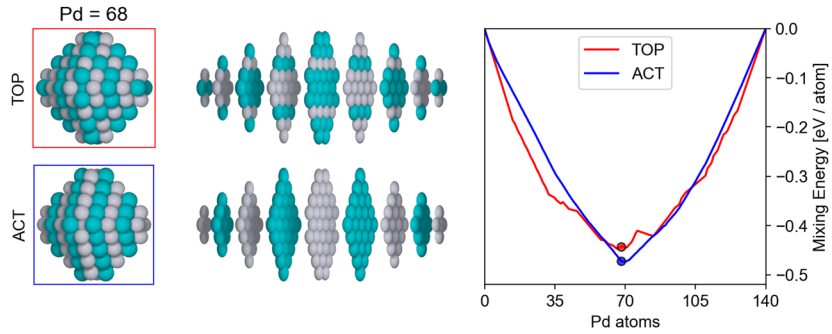

FIG. 11. Single frame of the supplementary material movie that shows the evolution of the PdZn chemical ordering along the mixing energy convex hull. Each NP is represented in its entirety and as separated layers. TOP and ACT mixing energy convex hulls are depicted in red and blue lines in the plot. The points in the graph indicate the positions of the depicted particles in the convex hull (Multimedia available online).

different minima found are not characterized by the presence of seldom sampled atom types.

Analyzing the convex hull in more detail reveals that the lowest E_{mix} structure corresponds to the $Pd_{72}Zn_{68}$ stoichiometry, which allows for a perfectly layered chemical ordering, as expected. This structure and stoichiometry are followed in terms of stability by the perfectly layered $Pd_{68}Zn_{72}$, which results from inverting the layers of the most stable $Pd_{72}Zn_{68}$ structure. The evolution of the chemical ordering and E_{mix} as a function of the composition can be more clearly appreciated in Fig. 11 (Multimedia view). This figure and video illustrate the global minima produced by TOP and ACT at each stoichiometry, shown either whole (left panels) or divided into layers (middle panels). The video shows that initially up to 12 Zn atoms occupy bulk positions. Here, we observe the first difference between the TOP and ACT models: the TOP model places Zn in the bulk and maximizes Pd–Zn bonds, while ACT starts placing Zn on the surface and forming square motifs next to the corner, as seen in $Pd_{122}Zn_{18}$. We conclude that ACT is producing the lowest-energy chemical ordering in this composition region based on the data in Fig. 10. The first indications of the trend to layering in the chemical ordering appear at $Pd_{84}Zn_{56}$ for both models. However, only ACT is able to capture the perfectly layered structure of both $Pd_{72}Zn_{68}$, which is at the minimum of the convex hull, and $Pd_{68}Zn_{72}$, corresponding to the structure with inverse layering. The behavior of Pd at low Pd concentrations is similar to that of Zn at low Zn concentrations; the more dilute metal tends to occupy the bulk positions, but still occupies some surface positions of the NP.

4. Surface sites of $Pd_{140-x}Zn_x$ (x = 1–139) nanoparticles and reactivity landscape

Having determined the most stable homotops for every $Pd_{140-x}Zn_x$ stoichiometry, we analyzed the nature of the surface sites exposed to reactants as a function of composition in $Pd_{140-x}Zn_x$ NPs, and how it affects the chemical (and therefore catalytic) properties of these nanoalloys. Figure 12 illustrates the concentration of the various surface on-top, bridge, and threefold hollow sites as a function of the number of Pd atoms in the NP. These concentrations evolve as expected, with higher ratios of surface Pd sites as the concentration of Pd in the particle increases. Since the most stable chemical orderings correspond to layered or quasi-layered structures and there is no pronounced preference for one of the two metals to occupy surface positions, the surface site concentrations exhibit a practically symmetrical evolution around the 1:1 stoichiometry. The site concentrations predicted by TOP and ACT are very similar from ~Pd_1Zn_{139} to $Pd_{30}Zn_{110}$ and from ~$Pd_{125}Zn_{15}$

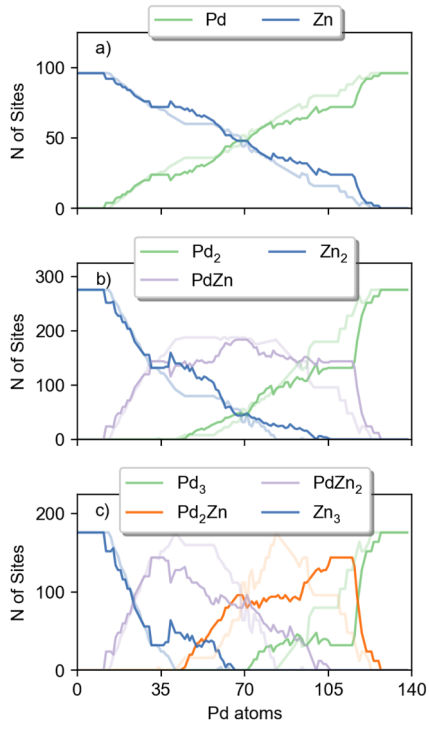

FIG. 12. Adsorption site-type concentration analysis of global minimum nanoparticles at varying compositions obtained using ACT (opaque lines) and TOP (shaded lines) models as a function of Pd atoms in the nanoparticle. (a) Concentration of on-top (singleton) Pd and Zn sites; (b) concentration of bridge (dimer) Pd_2, PdZn, and Zn_2 sites; and (c) concentration of threefold hollow (trimer) Pd_3, Pd_2Zn, $PdZn_2$, and Zn_3 sites.

to $Pd_{139}Zn_1$, but differ more from ~$Pd_{31}Zn_{109}$ to $Pd_{120}Zn_{20}$. In general, ACT GMs exhibit more Zn and fewer Pd surface sites than TOP GMs, which is reflected in ACT predicting a higher concentration of surface on-top Zn and bridge Zn_2 and Zn_3 surface sites. In addition, the concentration of heterometallic PdZn, $PdZn_2$, and Pd_2Zn sites increases and decreases more abruptly with the number of Pd atoms for the TOP GMs, also reaching higher maximum values. As we show below, the surface composition differences predicted by the two models result in significantly differing reactivity.

The distribution of surface sites as a function of composition described above determines the chemical and catalytic properties of the PdZn NPs. A full characterization of the reactivity landscape of such particles is, however, unfeasible directly with DFT calculations—calculating the adsorption energy of a single adsorbate on every possible adsorption site of just 30 structures (minima) of the convex hull involves ~16k geometry optimizations. This large computational effort can be partially circumvented by recently developed machine-learning models able to predict the adsorption energies for different adsorbates and/or carry out geometry optimizations with a trained interatomic potential.[92–94] Notably, several such ML-models participate in the Open Catalyst Project,[93,94] where their accuracy is evaluated and compared for a large dataset of millions of adsorption energies on different metal and oxide surfaces. To illustrate how to relate the identified chemical ordering global minima of the NPs to their electrocatalytic properties, we have carefully selected the pretrained paiNN ML model able to describe adsorption on the PdZn particles (see details in the supplementary material[95]). With this ML model, we have calculated the adsorption energy of an electrocatalytically relevant intermediate for the hydrogen evolution reaction (HER) on all sites of the minima that the TOP and ACT models identified for the 15 stoichiometries selected in Sec. III C. We should note, however, that this analysis was performed as a proof of concept of the potential of combining ML potentials and our chemical ordering optimization approaches, rather than suggesting PdZn nanoalloys as promising catalysts for the HER. In fact, Zn atoms are likely to dissolve upon operating conditions of the HER.[96]

We evaluated the hydrogen evolution reactivity of PdZn NPs using a reductionist approach that relies on just a single descriptor. This descriptor, proposed by Norskov and co-workers,[97] is the adsorption energy of H, $E_{ads}(H)$, which correlates strongly with the HER exchange current and results in the well-known volcano-type dependency. The tip of the volcano, which is associated with the highest HER activity, is found at $E_{ads}(H) = -0.24$ eV (calculated at the DFT level of theory with the PBE exchange–correlation functional).

The distribution of adsorption energies calculated for the selected $Pd_{140-x}Zn_x$ NPs is shown as violin plots in Fig. 13 for different site-types [Fig. 13(a)] and NP stoichiometries [Fig. 13(b)]. The adsorption energy distribution for TOP and ACT GMs is shown on each side of the violin plots. Three dotted lines inside each distribution indicate the median and 1.5 times the interquartile range, and the number of entries in each distribution is indicated below every site-type and stoichiometry label. Note that we only display ~ 7k (3.3k for ACT and 3.9k for TOP) adsorption energy values (out of a total of 16.6k evaluated sites) for which the H adsorbate did not migrate to other sites upon relaxation. The H adsorbate was considered migrated from the initial adsorption site guess when the number of neighbors changed upon relaxation. The number of neighbors was obtained by considering bond length thresholds of

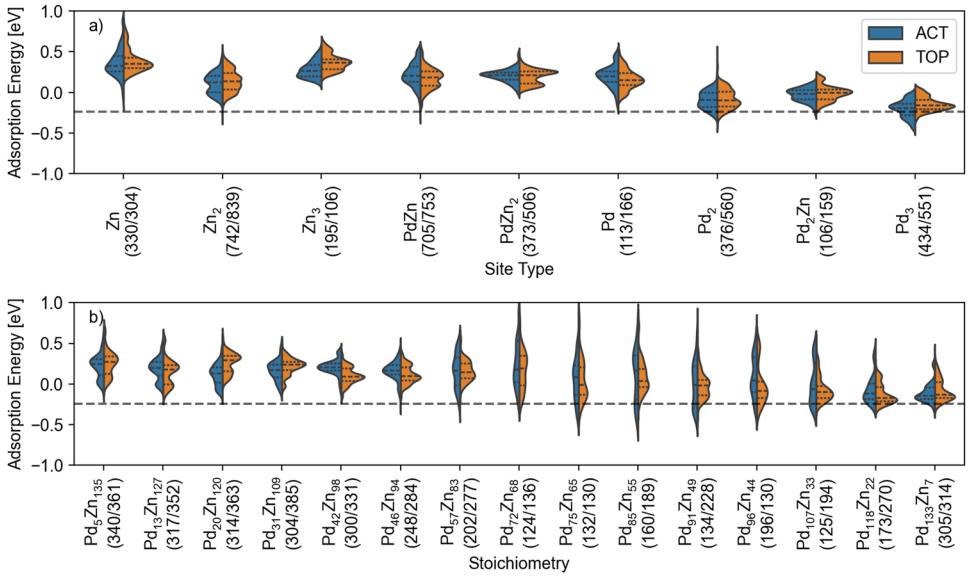

FIG. 13. Violin plot distribution of adsorption energies of H as a function of site type (a) and nanoparticle composition (b) for global minimum structures obtained with ACT (blue) and TOP (orange). The top and bottom tips of the violin correspond to the maximum and minimum values of the distribution, respectively. The area enclosed between the dotted lines delimits the values corresponding to 1.5 times the interquartile range, while the middle line indicates the median of the distribution. The number of adsorption sites in each distribution (those where H did not migrate to other sites upon relaxation) is indicated in parentheses for ACT (low) and TOP (top) and was used to normalize each distribution. The horizontal dashed line marks the adsorption energy associated with the highest activity.

2.29 and 2.12 Å for Pd–H and Zn–H bonds, respectively, derived from the natural covalent radii as implemented in the Atomic Simulation Environment.

The E_{ads}(H) distributions in Fig. 13(a) are broader for on-top sites and narrower for threefold sites. This is expected, since the reactivity of single Zn and Pd atoms is more affected by the environment than that of sites formed by three atoms. This also indicates that describing each site only by the nature of the atoms directly contacting the adsorbate is better suited for threefold sites, but too simplistic for on-top sites. Further differentiation by considering, for example, coordination numbers should lead to narrower site-type E_{ads} distributions. Overall, the E_{ads}(H) distributions for different site types are very similar for TOP and ACT GMs. In general, sites with lower Zn content bind H more strongly, with threefold Pd_3 sites binding H most strongly. Importantly, E_{ads}(H) distributions for hollow Pd_3 sites are closest to the ideal HER value, implying that particles with maximized concentrations of such sites are more active.

Different chemical orderings predicted by the TOP and ACT models cause pronounced differences in E_{ads}(H) distributions for many NP stoichiometries [Fig. 13(b)], which illustrates how the chemical ordering influences the reactivity of a nanoalloy. These effects are more evident for systems with high Zn and low Pd content, for which the TOP model overestimates the concentrations of surface Pd. For NPs with a higher Pd content, ACT models generally lead to broader E_{ads}(H) distributions. As a result, ACT predicted minima have distributions with bottom tails that cross the ideal E_{ads}(H) for the stoichiometries ranging from $Pd_{76}Zn_{64}$ to $Pd_{134}Zn_6$, indicating the presence of potentially highly active sites for all these compositions. The count of highly active sites, characterized by an adsorption energy of -0.24 ± 0.1 eV, is reported in Table S2. This is in part due to the emergence of surface Pd_3 starting at $Pd_{76}Zn_{64}$ [see Fig. 12(c)], as well as some Pd_2 sites with low E_{ads}(H). The emergence of Pd_3 as the most promising sites in Fig. 13(a) suggests that particles maximizing the concentration of surface Pd sites would be most active. Although this corresponds to NPs with the highest Pd content, the E_{ads}(H) distribution of NPs with stoichiometries from $Pd_{96}Zn_{44}$ to $Pd_{133}Zn_7$ is very similar. Therefore, although addition of Zn to Pd particles does not improve the HER activity, small amounts of Zn of up to 30% would have little effect on the single-metal activity, indicating that addition of Zn could be a suitable strategy to reduce the catalyst cost without compromising activity, i.e., by increasing the activity per used Pd atom.

IV. CONCLUSIONS

In this work, we have evaluated the accuracy, data-efficiency, transferability, and performance in global optimization approaches of various surrogate energy models for bimetallic (fcc) nanoalloys. We have compared models based on coordination- and/or bond-centered descriptors, including the widely used topological (TOP) method[50–59] and a newly proposed descriptor based on atomic coordination types (ACTs). Nanoalloys exhibiting stable segregated core–shell (PtAu), well-mixed (PtCu), and layered (PdZn) chemical orderings have been addressed.

Our results show that bond descriptors outperform coordination descriptors in predicting the energy of bimetallic nanoparticles. Combining both bonding- and coordination-descriptors, giving rise to the as-originally formulated TOP approach and extensions of it, further improves the model performance. We note that such extensions (consisting in adding more bonding or coordination descriptors to the original TOP) just slightly reduce prediction errors but spoil the interpretability of the regression coefficients. Whereas for the simpler models, these coefficients agree well with the trends in chemical ordering exhibited by the different nanoalloys, coefficients from more complex models lack a straightforward meaning.

Surrogate energy models relying on the ACT descriptors were found to be more accurate than the original TOP approach and its extensions, with prediction errors ca. twice smaller. However, ACT models are less data-efficient than TOP ones and require significantly more training examples to converge; in addition, the regression coefficients cannot be reliably interpreted. Nevertheless, when converged, ACT models partially overcome limitations of the TOP approach to properly distinguish chemical orderings in the bulk regions of nanoalloys. These limitations arise from the non-uniqueness of the TOP descriptor and its focus on surface structural features (e.g., the number of under-coordinated atoms of a given element). The ACT descriptor is also non-unique, although less significantly than for the TOP descriptors.

The TOP models are more transferable across stoichiometries than the ACT model. A TOP model trained in one stoichiometry performs better than the ACT model in predicting the stability of homotops of other stoichiometries. This is due to some atomic coordinated types being present only in some stoichiometries, resulting in very inaccurate regression coefficients for predictions of the energy of NPs containing atomic coordination types not appearing in the training set.

Both TOP and ACT models can be combined with various global optimization approaches, including a recently developed optimal exchange algorithm that relies on local energy expressions derivable from both TOP and ACT SEMs. The complexity of the SEM is, however, not consistently related to improved efficiency in terms of the number of SEM energy evaluations required to find the global minimum during a search. In turn, the type of mixing exhibited by global minimum chemical ordering strongly affects the number of candidates that need to be evaluated to find it, with well-mixed nanoalloys representing more challenging search problems than for nanoalloys with core–shell orderings.

Finally, we have applied both TOP and ACT models to the description of PdZn nanoalloys, using a database of 600 $Pd_{140-x}Zn_x$ structures whose energies were calculated at the DFT level of theory. The energy prediction errors for this set are also lower for ACT than for TOP, but significantly larger than for the PtAu and PtCu systems. This is due to the much stronger interactions between Pd and Zn than between the metals comprising the other studied nanoalloys.

ACT descriptors therefore overcome some of the limitations of TOP descriptors in reliably describing chemical ordering of bulk-like regions of bimetallic nanoparticles. As such, this method will improve our understanding of well-mixed metal combinations (such as intermetallics), where the ordering of bulk-like regions is crucial to the resulting chemical and catalytic properties. For this system, a surface site analysis has allowed us to describe the relative abundance of different adsorption sites as a function of nanoalloy composition. Combining this with an ML-model describing adsorbate–surface interactions has therefore provided a detailed picture of the distribution of adsorption energies on PdZn nanoparticles as a function

of the Pd:Zn ratio, which allows identifying promising systems and site-types for the Hydrogen Evolution Reaction (HER). Our results show that mixing of Zn and Pd in bimetallic nanoparticles leads to a distribution of H adsorption energies that, according to reductionist descriptions of HER activity, should be as active as single metal Pd particles. These active NPs expose hollow Pd_3 sites exhibiting close to optimal E_{ads}(H) values. This therefore represents an advanced approach for the computational screening of bimetallic catalysts, further facilitated by the implementation of these methods in the newly developed and open-source nanoparticle library (https://github.com/reac-nps/NanoParticleLibrary.git).[86]

SUPPLEMENTARY MATERIAL

The supplementary material includes additional figures and descriptions regarding ACT SEM transferability, atom-type makeup of the training set and selected minima, and calibration of the ML adsorption model. A video is also available illustrating the evolution of the chemical ordering of the $Pd_{140-x}Zn_x$ NP along the convex hull, of which Fig. 11 is a single frame.

ACKNOWLEDGMENTS

This work was supported by the Spanish/FEDER *Ministerio de Ciencia, Innovación y Universidades* [Grant Nos. PID2021-128217NB-I00, MDM-2017-0767, CEX2021-001202-M, PID2022-140120OA-I00, and RYC2021-032281-I (for A.B.)] as well as by the *Generalitat de Catalunya* [Grant Nos. 2018BP00190 (for A.B.) and 2021SGR00286]. A.B. also acknowledges the support of the Junior Leader Program from "La Caixa Foundation." K.M.N. thanks Professor Libuda and Professor Görling for their hospitality at the CLINT Center (FAU-Erlangen, Germany) during the preparation of this article for publication. Computer resources have been partly provided by the Red Española de Supercomputación. This study was also supported by the European COST Actions CA18234 and CA21101.

AUTHOR DECLARATIONS

Conflict of Interest

The authors have no conflicts to disclose.

Author Contributions

Riccardo Farris: Conceptualization (equal); Data curation (equal); Formal analysis (lead); Investigation (lead); Methodology (lead); Software (lead); Visualization (lead); Writing – original draft (lead); Writing – review & editing (supporting). **Konstantin M. Neyman**: Funding acquisition (lead); Project administration (equal); Resources (lead); Supervision (equal); Writing – review & editing (equal). **Albert Bruix**: Conceptualization (lead); Data curation (equal); Methodology (equal); Project administration (lead); Supervision (lead); Writing – review & editing (lead).

DATA AVAILABILITY

The implemented algorithms (along with tutorials) are available in the newly developed and open-source nanoparticle library (https://github.com/reac-nps/NanoParticleLibrary.git). The DFT data that support the findings of this study are openly available in the ioChem-BD repository at http://doi.org/10.19061/iochem-bd-6-351.[98]

REFERENCES

[1] R. Ferrando, J. Jellinek, and R. L. Johnston, "Nanoalloys: From theory to applications of alloy clusters and nanoparticles," Chem. Rev. **108**, 845–910 (2008).
[2] F. Calvo, *Nanoalloys: From Fundamentals to Emergent Applications* (Elsevier, 2013).
[3] M. Gaudry *et al.*, "Size and composition dependence in the optical properties of mixed (transition metal/noble metal) embedded clusters," Phys. Rev. B **67**, 155409–155410 (2003).
[4] K. Sumiyama *et al.*, "Structural evolution and magnetic properties of nanogranular metallic alloys," J. Non-Cryst. Solids **192–193**, 539–545 (1995).
[5] D. Astruc, "Introduction: Nanoparticles in catalysis," Chem. Rev. **120**, 461–463 (2020).
[6] Y. He *et al.*, "Size-dependent dynamic structures of supported gold nanoparticles in CO oxidation reaction condition," Proc. Natl. Acad. Sci. U. S. A. **115**, 7700–7705 (2018).
[7] N. Hodnik *et al.*, "Effect of ordering of $PtCu_3$ nanoparticle structure on the activity and stability for the oxygen reduction reaction," Phys. Chem. Chem. Phys. **16**, 13610–13615 (2014).
[8] F. Calvo, E. Cottancin, and M. Broyer, "Segregation, core alloying, and shape transitions in bimetallic nanoclusters: Monte Carlo simulations," Phys. Rev. B **77**, 121406–121414 (2008).
[9] Q. Jia *et al.*, "Roles of Mo surface dopants in enhancing the ORR performance of octahedral PtNi nanoparticles," Nano Lett. **18**, 798–804 (2018).
[10] G. Rossi, R. Ferrando, and C. Mottet, "Structure and chemical ordering in CoPt nanoalloys," Faraday Discuss. **138**, 193–210 (2008).
[11] N. Artrith and A. M. Kolpak, "Grand canonical molecular dynamics simulations of Cu-Au nanoalloys in thermal equilibrium using reactive ANN potentials," Comput. Mater. Sci. **110**, 20–28 (2015).
[12] J. Weinreich, A. Römer, M. L. Paleico, and J. Behler, "Properties of α-brass nanoparticles. 1. Neural network potential energy surface," J. Phys. Chem. C **124**, 12682–12695 (2020).
[13] R. L. Johnston, "Evolving better nanoparticles: Genetic algorithms for optimising cluster geometries," Dalton Trans. **3**, 4193–4207 (2003).
[14] G. Shao *et al.*, "An improved genetic algorithm for structural optimization of Au–Ag bimetallic nanoparticles," Appl. Soft Comput. **73**, 39–49 (2018).
[15] L. B. Vilhelmsen and B. Hammer, "A genetic algorithm for first principles global structure optimization of supported nano structures," J. Chem. Phys. **141**, 044711 (2014).
[16] J. Q. Goh, J. Akola, and R. Ferrando, "Geometric structure and chemical ordering of large AuCu clusters: A computational study," J. Phys. Chem. C **121**, 10809–10816 (2017).
[17] F. Calvo, N. Combe, J. Morillo, and M. Benoit, "Modeling iron-gold nanoparticles using a dedicated semi-empirical potential: Application to the stability of core-shell structures," J. Phys. Chem. C **121**, 4680–4691 (2017).
[18] C. A. Casey-Stevens *et al.*, "A theoretical investigation of 38-atom CuPd clusters: The effect of potential parameterisation on structure and segregation," Phys. Chem. Chem. Phys. **23**, 15950–15964 (2021).
[19] R. Du *et al.*, "Theoretical study of the structures of bimetallic Ag–Au and Cu–Au clusters up to 108 atoms," R. Soc. Open Sci. **6**, 190342 (2019).
[20] R. P. Gupta, "Lattice relaxation at a metal surface," Phys. Rev. B **23**, 6265–6270 (1981).
[21] K. W. Jacobsen, P. Stoltze, and J. K. Nørskov, "A semi-empirical effective medium theory for metals and alloys," Surf. Sci. **366**, 394–402 (1996).
[22] M. S. Daw and M. I. Baskes, "Embedded-atom method: Derivation and application to impurities, surfaces, and other defects in metals," Phys. Rev. B **29**, 6443–6453 (1984).
[23] J. Weinreich, M. L. Paleico, and J. Behler, "Properties of α-brass nanoparticles II: Structure and composition," J. Phys. Chem. C **125**, 14897–14909 (2021).

[24]N. Artrith and A. Urban, "An implementation of artificial neural-network potentials for atomistic materials simulations: Performance for TiO_2," Comput. Mater. Sci. **114**, 135–150 (2016).
[25]T. Roongcharoen *et al.*, "Oxidation and de-alloying of PtMn particle models: A computational investigation," Faraday Discuss. **242**, 174–192 (2023).
[26]S. Han *et al.*, "Unfolding the structural stability of nanoalloys via symmetry-constrained genetic algorithm and neural network potential," npj Comput. Mater. **8**, 121–211 (2022).
[27]J. Behler and M. Parrinello, "Generalized neural-network representation of high-dimensional potential-energy surfaces," Phys. Rev. Lett. **98**, 146401–146404 (2007).
[28]J. Behler, "Atom-centered symmetry functions for constructing high-dimensional neural network potentials," J. Chem. Phys. **134**, 074106 (2011).
[29]N. Artrith, A. Urban, and G. Ceder, "Efficient and accurate machine-learning interpolation of atomic energies in compositions with many species," Phys. Rev. B **96**, 014112–014115 (2017).
[30]L. Himanen *et al.*, "DScribe: Library of descriptors for machine learning in materials science," Comput. Phys. Commun. **247**, 106949 (2020).
[31]F. Musil *et al.*, "Physics-inspired structural representations for molecules and materials," Chem. Rev. **121**, 9759–9815 (2021).
[32]D. Fioravanti, G. Barcaro, and A. Fortunelli, "An augmented (multi-descriptor) grouping algorithm to optimize chemical ordering in nanoalloys," Phys. Chem. Chem. Phys. **23**, 23075–23089 (2021).
[33]J. Behler, "Representing potential energy surfaces by high-dimensional neural network potentials," J. Phys. Condens. Matter **26**, 183001 (2014).
[34]Z. Yan, M. G. Taylor, A. Mascareno, and G. Mpourmpakis, "Size-shape-and composition-dependent model for metal nanoparticle stability prediction," Nano Lett. **18**, 2696–2704 (2018).
[35]J. Dean, M. J. Cowan, J. Estes, M. Ramadan, and G. Mpourmpakis, "Rapid prediction of bimetallic mixing behavior at the nanoscale," ACS Nano **14**, 8171–8180 (2020).
[36]D. J. Loevlie, B. Ferreira, and G. Mpourmpakis, "Demystifying the chemical ordering of multimetallic nanoparticles," Acc. Chem. Res. **56**, 248–257 (2023).
[37]L. T. Roling, L. Li, and F. Abild-Pedersen, "Configurational energies of nanoparticles based on metal-metal coordination," J. Phys. Chem. C **121**, 23002–23010 (2017).
[38]L. T. Roling and F. Abild-Pedersen, "Structure-sensitive scaling relations: Adsorption energies from surface site stability," ChemCatChem **10**, 1643–1650 (2018).
[39]L. T. Roling, T. S. Choksi, and F. Abild-Pedersen, "A coordination-based model for transition metal alloy nanoparticles," Nanoscale **11**, 4438–4452 (2019).
[40]J. M. Sanchez, F. Ducastelle, and D. Gratias, "Generalized cluster description of multicomponent systems," Physica A **128**, 334–350 (1984).
[41]M. Ångqvist *et al.*, "ICET – A Python library for constructing and sampling alloy cluster expansions," Adv. Theory Simul. **2**, 1–10 (2019).
[42]X. Huang *et al.*, "High-performance transition metal–doped Pt_3Ni octahedra for oxygen reduction reaction," Science **348**, 1230 (2015).
[43]C. Li *et al.*, "Improved prediction of nanoalloy structures by the explicit inclusion of adsorbates in cluster expansions," J. Phys. Chem. C **122**, 18040–18047 (2018).
[44]L. Cao, C. Li, and T. Mueller, "The use of cluster expansions to predict the structures and properties of surfaces and nanostructured materials," J. Chem. Inf. Model. **58**, 2401–2413 (2018).
[45]T. Eom *et al.*, "Cluster expansion method for simulating realistic size of nanoparticle catalysts with an application in CO_2 electroreduction," J. Phys. Chem. C **122**, 9245–9254 (2018).
[46]P. M. Larsen, K. W. Jacobsen, and J. Schiøtz, "Rich ground-state chemical ordering in nanoparticles: Exact solution of a model for Ag-Au clusters," Phys. Rev. Lett. **120**, 256101 (2018).
[47]B. C. Han, A. Van Der Ven, G. Ceder, and B. J. Hwang, "Surface segregation and ordering of alloy surfaces in the presence of adsorbates," Phys. Rev. B **72**, 205409 (2005).
[48]G. Kovács, S. M. Kozlov, and K. M. Neyman, "Versatile optimization of chemical ordering in bimetallic nanoparticles," J. Phys. Chem. C **121**, 10803–10808 (2017).
[49]S. M. Kozlov, G. Kovács, R. Ferrando, and K. M. Neyman, "How to determine accurate chemical ordering in several nanometer large bimetallic crystallites from electronic structure calculations," Chem. Sci. **6**, 3868–3880 (2015).
[50]M. Vorokhta *et al.*, "Surface composition of magnetron sputtered Pt-Co thin film catalyst for proton exchange membrane fuel cells," Appl. Surf. Sci. **365**, 245–251 (2016).
[51]G. Kovács *et al.*, "Revealing chemical ordering in Pt-Co nanoparticles using electronic structure calculations and X-ray photoelectron spectroscopy," Phys. Chem. Chem. Phys. **17**, 28298–28310 (2015).
[52]A. Wolfbeisser *et al.*, "Surface composition changes of CuNi-ZrO_2 during methane decomposition: An operando NAP-XPS and density functional study," Catal. Today **283**, 134–143 (2017).
[53]I. Khalakhan *et al.*, "Irreversible structural dynamics on the surface of bimetallic PtNi alloy catalyst under alternating oxidizing and reducing environments," Appl. Catal., B **264**, 118476 (2020).
[54]A. Neitzel *et al.*, "Atomic ordering and Sn segregation in Pt–Sn nanoalloys supported on CeO_2 thin films," Top. Catal. **60**, 522–532 (2017).
[55]L. Vega, H. A. Aleksandrov, and K. M. Neyman, "Using density functional calculations to elucidate atomic ordering of Pd-Rh nanoparticles at sizes relevant for catalytic applications," Chin. J. Catal. **40**, 1749–1757 (2019).
[56]M. Mamatkulov *et al.*, "Pd segregation on the surface of bimetallic PdAu nanoparticles induced by low coverage of adsorbed CO," J. Phys. Chem. C **123**, 8037–8046 (2019).
[57]S. Olobardi *et al.*, "Optical properties and chemical ordering of Ag-Pt nanoalloys: A computational study," J. Phys. Chem. C **123**, 25482–25491 (2019).
[58]M. Mamatkulov, I. V. Yudanov, A. V. Bukhtiyarov, and K. M. Neyman, "Pd single-atom sites on the surface of pdau nanoparticles: A DFT-based topological search for suitable compositions," Nanomaterials **11**, 122–217 (2021).
[59]X. Xie *et al.*, "Optimal Pt-Au alloying for efficient and stable oxygen reduction reaction catalysts," ACS Appl. Mater. Interfaces **15**, 1192–1200 (2022).
[60]N. Artrith *et al.*, "Best practices in machine learning for chemistry," Nat. Chem. **13**, 505–508 (2021).
[61]J. Luo *et al.*, "Characterization of carbon-supported AuPt nanoparticles for electrocatalytic methanol oxidation reaction," Langmuir **22**, 2892–2898 (2006).
[62]M. Schrinner *et al.*, "Single nanocrystals of platinum prepared by partial dissolution of Au-Pt nanoalloys," Science **323**, 617–620 (2009).
[63]J. Zhang, G. Chen, D. Guay, M. Chaker, and D. Ma, "Highly active PtAu alloy nanoparticle catalysts for the reduction of 4-nitrophenol," Nanoscale **6**, 2125–2130 (2014).
[64]T. Liu *et al.*, "Monodispersed sub-5.0 nm PtCu nanoalloys as enhanced bifunctional electrocatalysts for oxygen reduction reaction and ethanol oxidation reaction," Nanoscale **9**, 2963–2968 (2017).
[65]Q. Liu *et al.*, "Synthesis of CuPt nanorod catalysts with tunable lengths," J. Am. Chem. Soc. **131**, 5720–5721 (2009).
[66]C. M. Zhu, A. Gao, Y. Wang, and Y. Liu, "Pt-Cu bimetallic electrocatalysts with enhanced catalytic properties for oxygen reduction," Chem. Commun. **50**, 13889–13892 (2014).
[67]M. A. Matin *et al.*, "PdZn nanoparticle electrocatalysts synthesized by solution combustion for methanol oxidation reaction in an alkaline medium," RSC Adv. **7**, 42709–42717 (2017).
[68]K. Föttinger, "PdZn based catalysts: Connecting electronic and geometric structure with catalytic performance," Catalysis **25**, 77 (2013).
[69]C. Liu *et al.*, "Promoting effect of PdZn alloy for selective hydrogenation of 5-hydroxylmethylfurfural: An experimental and density functional theory study," Int. J. Quantum Chem. **121**, e26545 (2021).
[70]A. H. Larsen, "The atomic simulation environment—A python library for working with atoms," J. Phys.: Condens. Matter **29**, 273002 (2017).
[71]G. Kresse and J. Hafner, "*Ab initio* molecular-dynamics simulation of the liquid-metal–amorphous-semiconductor transition in germanium," Phys. Rev. B **49**, 14251–14269 (1994).
[72]G. Kresse and J. Furthmüller, "Efficient iterative schemes for *ab initio* total-energy calculations using a plane-wave basis set," Phys. Rev. B **54**, 11169–11186 (1996).
[73]J. P. Perdew, K. Burke, and M. Ernzerhof, "Generalized gradient approximation made simple," Phys. Rev. Lett. **77**, 3865–3868 (1996).

[74]P. Janthon, S. M. Kozlov, F. Viñes, J. Limtrakul, and F. Illas, "Establishing the accuracy of broadly used density functionals in describing bulk properties of transition metals," J. Chem. Theory Comput. **9**, 1631–1640 (2013).
[75]P. Janthon *et al.*, "Bulk properties of transition metals: A challenge for the design of universal density functionals," J. Chem. Theory Comput. **10**, 3832–3839 (2014).
[76]L. Vega, J. Ruvireta, F. Viñes, and F. Illas, "Jacob's ladder as sketched by Escher: Assessing the performance of broadly used density functionals on transition metal surface properties," J. Chem. Theory Comput. **14**, 395–403 (2018).
[77]P. E. Blöchl, "Projector augmented-wave method," Phys. Rev. B **50**, 17953–17979 (1994).
[78]G. Kresse and D. Joubert, "From ultrasoft pseudopotentials to the projector augmented-wave method," Phys. Rev. B **59**, 1758–1775 (1999).
[79]F. Viñes, F. Illas, and K. M. Neyman, "On the mechanism of formation of metal nanowires by self-assembly," Angew. Chem., Int. Ed. **46**, 7094–7097 (2007).
[80]S. M. Kozlov, H. A. Aleksandrov, J. Goniakowski, and K. M. Neyman, "Effect of MgO(100) support on structure and properties of Pd and Pt nanoparticles with 49-155 atoms," J. Chem. Phys. **139**, 084701 (2013).
[81]G. L. W. Hart, T. Mueller, C. Toher, and S. Curtarolo, "Machine learning for alloys," Nat. Rev. Mater. **6**, 730–755 (2021).
[82]M. Ceriotti, C. Clementi, and O. Anatole Von Lilienfeld, "Introduction: Machine learning at the atomic scale," Chem. Rev. **121**, 9719–9721 (2021).
[83]M. Rupp, A. Tkatchenko, K. R. Müller, and O. A. Von Lilienfeld, "Fast and accurate modeling of molecular atomization energies with machine learning," Phys. Rev. Lett. **108**, 058301–058305 (2012).
[84]H. Huo and M. Rupp, "Unified representation of molecules and crystals for machine learning," Mach. Learn. Sci. Technol. **3**, 045017 (2022).
[85]F. Pedregosa *et al.*, "Scikit-learn: Machine learning in Python," J. Mach. Learn. Res. **12**, 2825–2830 (2011).
[86]F. Neumann, J. T. Margraf, K. Reuter, and A. Bruix, "Interplay between shape and composition in bimetallic nanoparticles revealed by an efficient optimal-exchange optimization algorithm," chemrxiv-2021-26ztp (2021).
[87]L. Vega *et al.*, "Chemical ordering in Pt-Au, Pt-Ag and Pt-Cu nanoparticles from density functional calculations using a topological approach," Mater. Adv. **2**, 6589–6602 (2021).
[88]Z. X. Chen, K. M. Neyman, A. B. Gordienko, and N. Rösch, "Surface structure and stability of PdZn and PtZn alloys: Density-functional slab model studies," Phys. Rev. B **68**, 075417 (2003).
[89]T. L. Jacobsen, M. S. Jørgensen, and B. Hammer, "On-the-Fly machine learning of atomic potential in density functional theory structure optimization," Phys. Rev. Lett. **120**, 026102 (2018).
[90]M. K. Bisbo and B. Hammer, "Efficient global structure optimization with a machine-learned surrogate model," Phys. Rev. Lett. **124**, 086102 (2020).
[91]R. Ferrando, A. Fortunelli, and G. Rossi, "Quantum effects on the structure of pure and binary metallic nanoclusters," Phys. Rev. B **72**, 085449 (2005).
[92]M. Andersen, S. V. Levchenko, M. Scheffler, and K. Reuter, "Beyond scaling relations for the description of catalytic materials," ACS Catal. **9**, 2752–2759 (2019).
[93]L. Chanussot *et al.*, "Open catalyst 2020 (OC20) dataset and community challenges," ACS Catal. **11**, 6059–6072 (2021).
[94]R. Tran *et al.*, "The open catalyst 2022 (OC22) dataset and challenges for oxide electrocatalysts," ACS Catal. **13**, 3066–3084 (2023).
[95]K. T. Schütt, O. T. Unke, and M. Gastegger, "Equivariant message passing for the prediction of tensorial properties and molecular spectra," in *International Conference on Machine Learning* (Proceedings of Machine Learning Research, 2021), Vol. 139.
[96]X. Guo and G. He, "Opportunities and challenges of zinc anodes in rechargeable aqueous batteries," J. Mater. Chem. A **11**, 11987–12001 (2023).
[97]J. K. Nørskov *et al.*, "Trends in the exchange current for hydrogen evolution," J. Electrochem. Soc. **152**, J23 (2005).
[98]M. Álvarez-Moreno *et al.*, "Managing the computational chemistry big data problem: The ioChem-BD platform," J. Chem. Inf. Model. **55**, 95–103 (2015).